Corti, R., Diambra, A., Muir Wood, D., Escribano Leiva, D., & Nash, D. (2016). Memory surface hardening model for granular soils under repeated loading conditions. *Journal of Engineering Mechanics*, *142*(12), [04016102-1]. https://doi.org/10.1061/(ASCE)EM.1943-7889.0001174

MEMORY SURFACE HARDENING MODEL FOR GRANULAR SOILS UNDER REPEATED LOADING CONDITIONS

Riccardo Corti. Ph.D. Student, Faculty of Engineering, Queen's Building, Univ. of Bristol, Bristol BS8 1TR, UK (corresponding author). E-mail: riccardo.corti@bristol.ac.uk

Andrea Diambra. Lecturer, Faculty of Engineering, Queen's Building, Univ. of Bristol, Bristol BS8 1TR, UK. E-mail: andrea.diambra@bristol.ac.uk

David Muir Wood. Emeritus Professor, Division of Civil Engineering Fulton Building, H13 University of Dundee Nethergate Dundee DD1 4HN, UK. E-mail: d.muirwood@dundee.ac.uk

Daniella E. Escribano. Lecturer, Faculty of Engineering, Department of Civil Engineering, Edmundo Larenas 215, Barrio Universitario, Conceptión, Chile. E-mail: describano@udec.cl

David F.T. Nash. Senior Research Fellow, Faculty of Engineering, Queen's Building, Univ. of Bristol, Bristol BS8 1TR, UK. E-mail: david.nash@bristol.ac.uk

Paper submitted for possible publication to:

Journal of Engineering Mechanics

ABSTRACT

The prediction of the stress-strain response of granular soils under large numbers of repeated loading cycles requires subtle changes to existing models, although the basic framework of kinematic hardening/bounding surface elasto-plasticity can be retained. Extending an existing model, an extra memory surface is introduced to track the stress history of the soil. The memory surface can evolve in size and position according to three rules which can be linked with physical principles of particle fabric and interaction. The memory surface changes in size and position through the experienced plastic volumetric strains but it always encloses the

current stress state and the yield surface; these simple rules permit progressive stiffening of the soil in cyclic loading, the accurate prediction of plastic strain rate accumulation during cyclic loading, and the description of slightly stiffer stress-strain response upon subsequent monotonic reloading. The implementation of the additional modelling features requires the definition of only two new constitutive soil parameters. A parametric analysis is provided to show model predictions for drained and undrained cyclic loading conditions. The model is validated against available tests on Hostun Sand performed under drained triaxial cyclic loading conditions with various confining pressures, densities, average stress ratios and cyclic amplitudes.

Keywords: **constitutive relations; fabric/structure of soils; friction; plasticity; cyclic loading; sands.**

Introduction

The accurate prediction of the mechanical response of granular soils subjected to large numbers of non-monotonic repeated loads is fundamental for the assessment of the serviceability and safety of many geotechnical engineering systems including foundations for road pavements (McVay and Taesiri, 1985), offshore structures such as wind turbines (Leblanc et al., 2009, Klinkvort and Hededal, 2013, Diambra et al. 2014) or oil and gas platforms (Randolph and Gourvenec, 2011) and foundations for vibrating or reciprocating machines among others. Currently available theoretical models for soil behaviour can capture the basic features of the non-monotonic cyclic behaviour of soil, such as progressive pore pressure generation for undrained conditions or progressive accumulation of plastic strain for drained loading. However, achieving a satisfactory quantitative accuracy for large numbers of repeated loads and effectively accounting for stress level and density conditions is still a challenging task.

The complexities of the response of a soil under cyclic loading are largely linked to the evolution of internal particulate fabric together with effective stress and/or density state. For loose or medium dense granular soils, cyclic straining causes densification and progressive evolution of particles into a more efficient packing. A more stable configuration is reached inducing a progressive increase in soil stiffness and reduction of further plastic strain accumulation (Wichtmann et al., 2005). Discrete element method (DEM) simulations of cyclic triaxial tests (O'Sullivan and Cui, 2009) have confirmed a redistribution of the relative magnitude of contact forces rather than a particles redistribution.

The most widespread constitutive approach to model the non-monotonic behaviour of soils is to incorporate kinematic hardening and/or bounding surface techniques (Mroz et al, 1978, Al-Tabbaa and Muir Wood, 1989, Manzari and Dafalias, 1997, Gajo and Muir Wood, 1999a). In these models the yield surface, enclosing the elastic states of the soil, moves to follow the

61 current stress state while the soil stiffness is generally proportional to the distance between
62 the current stress state and its image on the bounding surface. While reversed plasticity
63 during unloading, hysteretic behaviour and the progressive accumulation of plastic strains
64 with the number of cycles can be simulated, these models have no features specifically
65 intended to memorise the evolution of internal structure when the soil is subjected to repeated
66 cycles. The predictions that are obtained for cyclic loading tend to show a very steady
67 ratcheting behaviour; they are hardly affected by the small changes in specific volume during
68 cycling and they fail to reproduce the progressive changes of strain accumulation rate with
69 loading cycles. The stiffness of the sand hardly changes during the cycles.
70 Papadimitriou et al. (2001) and Papadimitriou and Bouckovalas (2002) also demonstrated the
71 need for additional modelling features to account for the evolution of soil fabric during cyclic
72 loading. They suggested that the evolution of plastic soil stiffness is affected by the
73 accumulated plastic volumetric strains during each loading cycle. Dafalias and Manzari
74 (2004) accounted for these changes by proposing a fabric-dilatancy tensor whose evolution is
75 governed by the plastic dilative volumetric strains; the trace of the fabric-dilatancy tensor
76 affects the flow rule of the model. Maleki et al. (2009) also implemented changes of the
77 hardening modulus and stress-dilatancy law between monotonic/virgin and cyclic loading
78 conditions. Within a multi-surface framework, Di Benedetto et al. (2014) proposed that a new
79 loading surface should be generated each time the load path underwent stress reversal while
80 all the previous loading surfaces were still memorised and the hardening modulus would be
81 affected by the normalised plastic shear work. A history surface has been implemented in a
82 three-surface model for clay (Stallebrass and Taylor, 1997) and more recently for sand
83 (Jafarzadeh et al., 2007) to account for the evolution of soil anisotropy while subjected to
84 non-monotonic loading in a cubical true triaxial cell.

A different modelling strategy is followed in this paper: the potential modelling benefits are explored of implementing an additional and evolving 'memory surface' to retain more information of stress history and somehow record the effect of repeated loading. The memory surface is a geometrical representation of the stress history and it bounds a region of stress states which the soil fabric 'feels' that it has already experienced. In contrast with other models, this memory surface is allowed to evolve both in size and position and thus simulate the changes in soil fabric during monotonic and repeated loading; the size and location of the memory surface may be a measure of the soil fabric and its anisotropy respectively. While in undrained cyclic conditions the change in effective stress generally has a dramatic effect on the soil stiffness and thus the soil response, the changes in soil density during drained cyclic loading appear to have less effect so that additional hardening mechanisms are necessary. Thus this paper concentrates on the ability of the proposed hardening mechanisms to capture the effects of soil fabric evolution during large numbers of drained cycles of loading. Simulations of drained cyclic and subsequent monotonic loading responses will be analysed for a range of densities, stress levels and cyclic amplitudes, while it will be demonstrated that the implemented modelling features enable also good simulations of the cyclic undrained response.

Basic concepts of proposed model

Description of the conceptual framework

The proposed modelling framework is built on a baseline soil model which broadly follows the kinematic hardening, bounding surface plasticity model proposed by Gajo and Muir Wood (1999a). A purely elastic region is bounded by the yield surface (f) which is a wedge with its apex at the origin of the q-p stress axes. When the soil stress state $\boldsymbol{\sigma}$ ($\boldsymbol{\sigma}=[q, p]^T$ where

q is the deviatoric stress and p is the mean effective stress) lies on the edge of the yield surface, the soil undergoes elasto-plastic deformation and a kinematic movement of the yield surface is imposed to satisfy the consistency condition. The possible stress states are bounded by a bounding surface (or strength surface F) whose opening is governed by a state parameter ψ (Been and Jefferies, 1985) which accounts for the difference in current specific volume (υ) and the respective one at critical state (υ_{csl}) for the current stress p:

$$\psi = \upsilon - \upsilon_{csl} \quad (1)$$

Different formulations have been proposed for the critical state line in the literature. If the stress range is limited, a linear formulation of the critical state line can be selected (Gajo and Muir Wood, 1999a). In this paper, the critical state line is assumed to be linear in the compression plane (υ-ln p) and the specific volume at the critical state is calculated as $\upsilon_{csl} = \upsilon_\lambda - \lambda \ln p$, where υ_λ and λ are two constitutive parameters defining the critical state specific volume for p=1 kPa and the slope of the critical state line (CSL), respectively. The strength surface approaches the critical state line as ultimate critical state conditions are asymptotically approached (Gajo and Muir Wood, 1999a) .

Fig. 1a provides an overview of model surfaces. The current value of the tangent plastic soil stiffness is dependent on the distance between the current stress state ($\boldsymbol{\sigma}$) and its image (or conjugate) stress ($\boldsymbol{\sigma}^{\boldsymbol{B}}$) on the bounding surface, defined in Fig. 1a. Adopting this framework to simulate soil response under drained cyclic loading conditions, plastic soil stiffness will only slightly vary upon consecutive cycles because of the limited changes in the soil state parameter (ψ) which affects the slope of the bounding surface. Soil behaviour is mostly governed by the state parameter if subjected to moderate to large shearing and soil fabric changes become of a second order importance. Thus the mechanical response between consecutive cycles will be rather similar and the changes in stiffness will be hardly noticeable. Evolution of model surfaces under such conditions and the corresponding stress-

135 strain response are presented in Fig. 1a and b, respectively. A further representation of the
136 model surfaces in the deviatoric stress space is proposed in Fig. 1c, where an Argyris shape
137 (Argyris et al., 1974) of the deviatoric section has been selected.
138
139 ***Additional model features: The memory surface and its evolution***
140 The memory surface is an additional wedge in the *q-p* stress plane which recalls the stress
141 states already experienced by the soil (Chow et al., 2015; Corti et al., 2015). When the
142 current stress state lies inside the memory surface, the memory surface f^M acts as an
143 additional bounding surface so that the plastic soil modulus is governed by an additional
144 hardening term depending on the distance between the current stress state and its projection
145 on the memory surface. This reproduces the experimentally observed stiffer soil behaviour
146 during repeated loading compared with virgin loading. Three rules describe the evolution of
147 the memory surface: Rule 1, the memory surface changes in size because of the experienced
148 plastic strains; Rule 2, the memory surface always encloses the current stress state; Rule 3,
149 the memory surface always encloses the current yield surface. Model response for simple
150 stress paths in both the triaxial stress space and the deviatoric stress space is presented in Fig.
151 2a-b-c-d. One can interpret the memory surface as a record of the current fabric of the soil,
152 describing the range of stresses that can be imposed without major disruptions to particle
153 arrangement. The yield surface indicates the stress changes that can be imposed with
154 essentially negligible interparticle movement.
155
156 <u>Rule 1: The memory surface changes in size with the plastic strains</u>
157 Positive plastic volumetric strains lead to a denser soil state which is generally related to a
158 more stable configuration and stronger soil fabric. It seems quite reasonable to associate
159 such conditions with an expansion of the memory surface as shown in Fig. 2a-b. In

contrast, it is postulated that negative (dilative) plastic volumetric strains produce a decrease in size of the memory surface which reproduces the loss of memory of some already experienced stress states (Fig. 2c-d). This last damage mechanism follows the experimental evidences by Tatsuoka et al (1997) who observed a decrease in soil stiffness, compared to virgin loading conditions, if large shearing or large amplitude cyclic loading was applied. Analogously, for cyclic loading under undrained conditions, a dramatic reduction in plastic stiffness can be observed when the load reversal is applied at high stress ratios (Ishihara et al., 1975, Georgiannou et al., 2008). Similarly to this proposal, Papadimitriou et al. (2001) and Papadimitriou and Bouckovalas (2002) introduced a damage to the soil fabric (leading to a reduction is plastic stiffness) when soil experiences dilative plastic volumetric strains.

Rule 2: The memory surface must always include the current stress state

Since the memory surface bounds a region of stress states which the soil fabric 'feels' that it has already experienced, the current stress state must always lie within its boundaries. During virgin loading conditions (when the current stress state is trying to explore an area outside the memory surface), the evolution of the memory surface must ensure that the current stress state lies on its boundaries as shown in Fig. 2a-b-c-d for both surface expansion and surface contraction.

Rule 3: The memory surface must always include the current yield surface

According to the interpretation of yield and memory surfaces given at the beginning of this section, it would be rather awkard to allow the yield to move outside the memory surface. The yield surface thus represents the miminum size of the memory surface and this requirement has to be considered in the contraction evolution law associated with negative plastic volumetric strains as shown in Fig. 2c-d.

185 Selected laws for the evolution of the memory surface which respect the three rules are
186 discussed in the following section.
187
188 **Mathematical formulation of the model**
189
190 ***The model surfaces***
191 The model assumes Mohr-Coulomb type failure conditions and the slope of the Critical State
192 Line M_{cs} is linked to the critical state friction angle ϕ_{cv} by the usual relationships:
193 $$M_{cs} = \frac{6 \sin \phi_{cv}}{3t - \sin \phi_{cv}} \quad (2)$$
194 where t assumes the value of +1 or -1 if shearing is occurring in compression ($M_{cs}=M_{cv}$) or
195 extension ($M_{cs}=M_{ev}$), respectively. Following the original development (Gajo and Muir Wood
196 1999a), the model is conveniently developed in a normalised stress space. The normalised
197 stress state is defined as:
198 $$\overline{\boldsymbol{\sigma}} = \begin{bmatrix} \frac{q}{r} \\ p \end{bmatrix} \quad (3)$$
199 where r is a function depending on the state parameter ψ (Eq. (1)) and expressed as:
200 $$r = 1 - k\psi \quad (4)$$
201 where k is a constitutive parameter. Some attention should be paid to the choice of the value
202 of k such that r remains positive for the investigated range of soil density. While the use of a
203 normalised stress space leads to a simplified and more elegant modelling formulation, the
204 validity of the proposed modelling strategy holds even if implemented in the conventional
205 stress space ($\boldsymbol{\sigma}=[q, p]^{T}$).
206 With state parameter defined in (1) and strength variation defined in (4) it is clear that the
207 normalising ratio r can become negative. Alternative defintions of ψ and r can be easily
208 adopted to avoid this problem (e.g. Li and Dafalias, 2000).

The bounding surface (F) is a wedge in the normalised stress space and its opening is equal to the critical state wedge opening, defined in Eq. (2):

$$F(\bar{\boldsymbol{\sigma}}) = \bar{\eta} - M_{cs} = 0 \tag{5}$$

where $\bar{\eta} = \bar{q}/p$ is the normalised stress ratio and $\bar{q} = q/r$.

The size of the yield surface is defined by the scalar m, representing the yield surface opening, that assumes the value m_c or m_e if the direction of shearing is heading towards compression or extension, respectively. The scalar m is proportional to the opening of the bounding surface M_{cs}

$$m = R|M_{cs}| \tag{6}$$

where R is a constitutive parameter. The yield surface (f) is expressed by:

$$f(\bar{\boldsymbol{\sigma}}, \boldsymbol{\alpha}) = \bar{\eta} - \alpha - t\, m = 0 \tag{7}$$

where the quantity $\alpha = \alpha_q/\alpha_p$, with α_q and α_p being the components of the unit direction vector of the centre of the yield surface $\boldsymbol{\alpha} = [\alpha_q, \alpha_p]^{\mathrm{T}}$. In the following development, the subscript $\square_q$ and $\square_p$ indicate deviatoric and isotropic components, respectively.

Following the described framework, the memory surface (f^M) is a wedge defined by opening angles $m^M = m_c^M$ and m_e^M in compression and extension, respectively, and the unit direction of the centre of the memory surface $\boldsymbol{\alpha}^M = [\alpha_q^M, \alpha_p^M]^{\mathrm{T}}$. Initially, when the stress state lies on the hydrostatic axes ($\bar{q} = 0$), the memory surface (f^M) is assumed to coincide with the yield surface but, as soon as the soil yields, the evolving stress history is followed through the evolution of the memory surface.

The memory surface is formulated as:

$$f^M(\bar{\boldsymbol{\sigma}}, \boldsymbol{\alpha^M}, m^M) = \bar{\eta} - \alpha^M - t\, m^M = 0 \tag{8}$$

with $\alpha^M = \alpha_q^M/\alpha_p^M$. A schematic representation of model surfaces is provided in Fig. 3a-b.

For consistency with the other model surfaces, the following relationship between the extension and compression sizes of the memory surface holds:

$$m_e^M / m_c^M = m_e / m_c \quad (9)$$

General elasto-plastic constitutive relationships

When the stress state lies inside the yield locus ($f(\bar{\boldsymbol{\sigma}}, \boldsymbol{\alpha}) < 0$), the soil obeys laws of isotropic elasticity and the incremental stress-strain relation ($\delta\boldsymbol{\sigma}$-$\delta\boldsymbol{\varepsilon}$, with $\boldsymbol{\varepsilon}$=[ε_q, ε_v]^T) becomes:

$$\delta\boldsymbol{\sigma} = \boldsymbol{D}^e \delta\boldsymbol{\varepsilon} = \begin{bmatrix} 3G & 0 \\ 0 & K \end{bmatrix} \delta\boldsymbol{\varepsilon} \quad (10)$$

where $\boldsymbol{D}^e$ is the elastic stiffness matrix and it is expressed in terms of elastic tangent shear modulus G and bulk modulus K. The normalised elastic stiffness matrix $\bar{\boldsymbol{D}}^e$, representing the elastic stiffness matrix in the normalised stress space, is calculated as:

$$\bar{\boldsymbol{D}}^{\boldsymbol{e}} = \begin{bmatrix} \frac{1}{1-k\psi} & \frac{k\lambda q}{(1-k\psi)^2 p} \\ 0 & 1 \end{bmatrix} \boldsymbol{D}^{\boldsymbol{e}} - \begin{bmatrix} 0 & \frac{kqv}{(1-k\psi)^2} \\ 0 & 0 \end{bmatrix} \quad (11)$$

When yielding occurs ($f(\bar{\boldsymbol{\sigma}}, \boldsymbol{\alpha}) = 0$), elasto-plastic conditions apply. The loading direction $\boldsymbol{n}$, representing the outward normal to the yield surface, is calculated from partial differentiation of Eq. (7)

$$\boldsymbol{n} = \begin{bmatrix} n_q \\ n_p \end{bmatrix} = \begin{bmatrix} t\frac{1}{\sqrt{1+\bar{\eta}^2}} \\ t\frac{-\bar{\eta}}{\sqrt{1+\bar{\eta}^2}} \end{bmatrix} \quad (12)$$

The dilatancy flow rule governing the evolution of the plastic strain increment ($\delta\boldsymbol{\varepsilon}^p$= [$\delta\varepsilon_q^p$, $\delta\varepsilon_v^p$]^T) and assumed to be non-associative, is of the following form:

$$d = \frac{\delta\varepsilon_v^p}{\delta\varepsilon_q^p} = A[M_{cs}(1 + k_d\psi) - \eta] \quad (13)$$

where the constitutive parameter A is a flow rule multiplier and k_d is a constitutive parameter governing the dependence of the plastic dilatancy on the state parameter. The outward normal of the plastic potential $\boldsymbol{m}$ is calculated directly from Eq. (13):

$$\boldsymbol{m} = \begin{bmatrix} m_q \\ m_p \end{bmatrix} = \begin{bmatrix} t\frac{1}{\sqrt{1+d^2}} \\ t\frac{d}{\sqrt{1+d^2}} \end{bmatrix} \quad (14)$$

Following the classical elasto-plasticity theory, the plastic strain increment vector can be defined as

$$\delta\boldsymbol{\varepsilon}^p = \frac{1}{H}\boldsymbol{m}\,\boldsymbol{n}^T\delta\bar{\boldsymbol{\sigma}} \tag{15}$$

From Eq. (15), the plastic volumetric strain increment is re-written as

$$\delta\varepsilon_v^p = \frac{1}{H}m_p p\; n_q\delta\bar{\eta} \tag{16}$$

where H is the hardening modulus which describes the required smooth (in general highly non-linear) stress-strain relationship.

For implementation in the normalised stress space, the unit vector $\boldsymbol{m}$ must be defined in this space by considering an extra small deviatoric component (Gajo and Muir Wood, 1999a)

$$\boldsymbol{m}^* = \boldsymbol{m} + \bar{\boldsymbol{D}}^{\boldsymbol{e}^{-1}}\begin{bmatrix}0 & \frac{kqv}{(1-k\psi)^2}\\ 0 & 0\end{bmatrix}\boldsymbol{m} \tag{17}$$

The stress-strain relationship $\delta\bar{\boldsymbol{\sigma}} - \delta\boldsymbol{\varepsilon}$ is finally defined by combining Eqs (10), (15) and (17) as

$$\delta\bar{\boldsymbol{\sigma}} = \bar{\boldsymbol{D}}^{ep}\delta\boldsymbol{\varepsilon} = \left[\bar{\boldsymbol{D}}^{\boldsymbol{e}} - \frac{\bar{\boldsymbol{D}}^{\boldsymbol{e}}\boldsymbol{m}^*\,\boldsymbol{n}^T\bar{\boldsymbol{D}}^{\boldsymbol{e}}}{H+\boldsymbol{n}^T\bar{\boldsymbol{D}}^{\boldsymbol{e}}\boldsymbol{m}^*}\right]\delta\boldsymbol{\varepsilon} \tag{18}$$

As shown in Fig. 2a-b the conjugate stress on the memory surface ($\bar{\boldsymbol{\sigma}}^M = [\bar{\eta}^M p, p]^T$, with $\bar{\eta}^M$ being the stress ratio associated with $\bar{\boldsymbol{\sigma}}^M$) and on bounding surface ($\bar{\boldsymbol{\sigma}}^B = [M_{cs}p, p]^T$) must be introduced (Fig. 3a). It should be noted that the conjugate stresses are calculated on the current deviatoric stress space (Fig. 3b).

The hardening modulus H is modified from the one proposed originally by Gajo and Muir Wood (1999a) to account for the inclusion of the memory surface through the distance b^M between the current stress state $\bar{\boldsymbol{\sigma}}$ and its image on the memory surface $\bar{\boldsymbol{\sigma}}^M$ (Fig. 3a-b):

$$H = \frac{b^2}{b_{max}{}_B}h \tag{19}$$

where h is an appropriate function to define the stiffness changes within the memory surface.

$$h = e^{\left(\frac{\mu b^M}{b}r\right)} \tag{20}$$

where $b = n_q[M_{cs}p - \bar{q}]$ is the distance between the current stress state ($\bar{\boldsymbol{\sigma}}$) and the conjugate one on the bounding surface ($\bar{\boldsymbol{\sigma}}^B$); $b^M = n_q[(\alpha^M + t\, m^M)p - \bar{q}]$ is the distance between the current stress state ($\bar{\boldsymbol{\sigma}}$) and the conjugate one on the memory surface ($\bar{\boldsymbol{\sigma}}^M$); $b_{max} = n_q t[M_{cv} + |M_{ev}|](1 - R)\, p$ (following Gajo and Muir Wood, 1999b) is the maximum value that b can assume; B and μ are two constitutive parameters governing the stress-strain response in monotonic and cyclic conditions, respectively and r is defined in Eq. (4). Although the hardening modulus H is always positive, the model can predict strain softening because of its implementation in the normalised stress space (Gajo and Muir Wood, 1999).

When the stress state lies on the memory surface (the distance b^M=0 and h=1), soil is in a virgin state and the original formulation of the hardening modulus employed by Gajo and Muir Wood (1999a) is re-established. In this case, the hardening modulus H is fully governed by the parameter B. Instead, when the stress state lies fully inside the memory surface (f^M), the constitutive parameter μ controls the increase in value of the hardening modulus H (through the term h) if compared to virgin loading conditions for the same stress state and size of the bounding surface. It should be noted that under non-monotonic loading conditions, the memory surface changes in size: an expansion of the memory surface leads to a progressive increase of the term h, leading to progressive increase of plastic soil stiffness; similarly, a reduction in size of the memory surface leads to a reduction in plastic soil stiffness.

Mathematical implementation of the rules for evolution of the memory surface

While the consistency condition of the yield surface can be found in Gajo and Muir Wood (1999a) (note the slightly different definition of the yield surface), in this paper more attention is given to the implementation of the memory surface. The evolution of the memory

surface is described by defining the translation of the memory surface centre $\boldsymbol{\alpha^M}$ and the changes in the memory surface size m^M.

Evolution of the memory surface opening

Following the described framework, when soil experiences plastic contractive volumetric strains, the memory surface expands (shown in Fig. 2a-b); whereas when soil experiences dilative plastic volumetric strains, the memory surface contracts (shown in Fig. 2c-d). The stress state and the yield surface must always lie on or inside the memory surface; this condition is particularly important for virgin conditions, where the memory surface evolves to accommodate the newly experienced stress state. Moreover, the condition of inclusion of the yield surface represents a limit to the contraction of the memory surface when soil experiences dilative plastic volumetric strains (Fig. 2c-d).

In order to develop an evolution rule for the memory surface, it may be convenient to imagine the expansion/contraction of the memory surface guided by the evolution of the image stress ($\boldsymbol{\bar{\sigma}^M}$). It should be noted that for virgin loading conditions, the image stress coincides with the current stress state. It is possible to rewrite Eq. (16) for the image stress and invert it to obtain a relastionship between plastic volumetric strains and change of the image ratio stress ($\bar{\eta}^M$).

$$\delta\bar{\eta}^M = \frac{H^M}{m_p p n_q}\delta\varepsilon_v^p \tag{21}$$

where H^M is the value of the hardening modulus if the stress state were coincident with the current image stress ($\boldsymbol{\bar{\sigma}^M}$):

$$H^M = \frac{\left(b-b^M\right)^2}{b_{max}B} \tag{22}$$

By assuming that the expansion of the memory surface is the result of a surface stretching to include the new image stress (but keeping the same shape) as shown in Fig. 2a-b, it is

possible to define the following evolution law for the opening of the surface in triaxial conditions:

$$\delta m^M = t\frac{z}{p\, n_q}\frac{H^M}{m_p}\delta\varepsilon_v^p \qquad (23)$$

where $z=|M_{cs}|/(M_{cv}+|M_{ev}|)$ and t are terms to consider whether the image stress is located on the compression or extension side of the memory surface. However, a further shrinkage of the surface should be allowed when plastic dilative strain takes place. An additional term for the size of the surface is then introduced to produce the following general expression for the evolution of the size of the surface:

$$\delta m^M = \frac{z}{p\, n_q}\left[t\frac{H^M}{m_p}\delta\varepsilon_v^p - \frac{b_{MAX}^M - b^M}{\varsigma}\langle -\delta\varepsilon_v^p\rangle\right] \qquad (24)$$

where ς is a constitutive parameter governing the memory surface contraction and the symbol $\langle A\rangle$ represents the Macaulay brackets ($\langle A\rangle=A$ if $A>0$ else $\langle A\rangle=0$). The quantity $b^M{}_{MAX}$-b^M is introduced to ensure that the memory surface never intersects the current yield surface. Similarly to b_{MAX}, $b^M{}_{MAX}$ is simply expressed as:

$$b_{MAX}^M = n_q t[m_c^M + m_e^M - m_c - m_e]\, p \qquad (25)$$

Equation (25) is the final expression of evolution for the size of the memory surface which is valid for all the loading conditions presented in Fig. 2a-b-c-d.

Translation of the memory surface centre

The translation of the memory surface centre $\boldsymbol{\alpha^M}$ follows the Mroz rule (Mroz, 1967, Yu, 2006) which assumes that the translation of the centre of a surface occurs along the vector joining the image stress on such surface and the image stress on the next surface. The direction of translation of the yield surface and memory surface can be observed in Fig. 3a in the triaxial stress space and in Fig. 3b in the deviatoric stress space. Following the Mroz rule, the evolution of the memory surface centre can be expressed as

$$\delta \boldsymbol{\alpha}^{\boldsymbol{M}} = \tau(\bar{\boldsymbol{\sigma}}^{\boldsymbol{B}} - \bar{\boldsymbol{\sigma}}^{\boldsymbol{M}}) \quad (26)$$

where τ is a scalar quantity. Eq. (26) must be slightly modified to ensure that the norm of $\boldsymbol{\alpha}^{\boldsymbol{M}}+\delta\boldsymbol{\alpha}^{\boldsymbol{M}}$ is unitary (Gajo and Muir Wood, 1999b)

$$\delta \boldsymbol{\alpha}^{\boldsymbol{M}} = \tau(\bar{\boldsymbol{\sigma}}^{\boldsymbol{B}} - \bar{\boldsymbol{\sigma}}^{\boldsymbol{M}}) - \tau[(\bar{\boldsymbol{\sigma}}^{\boldsymbol{B}} - \bar{\boldsymbol{\sigma}}^{\boldsymbol{M}})^T \boldsymbol{\alpha}^{\boldsymbol{M}}]\boldsymbol{\alpha}^{\boldsymbol{M}} \quad (27)$$

The consistency condition ensures that the image stress ($\bar{\boldsymbol{\sigma}}^{\boldsymbol{M}}$) remains on the memory surface:

$$\delta f^M(\bar{\boldsymbol{\sigma}}^{\boldsymbol{M}}, \boldsymbol{\alpha}^{\boldsymbol{M}}, m^M) = \left(\frac{\partial f^M}{\partial \bar{\boldsymbol{\sigma}}^{\boldsymbol{M}}}\right)^T \delta \bar{\boldsymbol{\sigma}}^{\boldsymbol{M}} + \left(\frac{\partial f^M}{\partial \boldsymbol{\alpha}^{\boldsymbol{M}}}\right)^T \delta \boldsymbol{\alpha}^{\boldsymbol{M}} + \frac{\partial f^M}{\partial m^M} \delta m^M = 0 \quad (28)$$

where

$$\delta \bar{\boldsymbol{\sigma}}^{\boldsymbol{M}} = \begin{bmatrix} \bar{\eta}^M \\ 1 \end{bmatrix} \delta p + \begin{bmatrix} p \\ 0 \end{bmatrix} \delta \bar{\eta}^M \quad (29)$$

It is now possible to define the scalar quantity τ by substituting Eq. (21) and Eq. (29) into Eq. (28) and then combining Eq. (28) and (27). The validity of this proposal has been checked for generalised multixial loading conditions. For the triaxial loading conditions of this paper, the evolution law of the centre of the surface becomes:

$$\delta \alpha^M = \frac{H^M}{m_p p n_q} \delta \varepsilon_v^p - t\, \delta m^M \quad (30)$$

Calibration of the model and effect of individual model parameters

Summary of constitutive model parameters

The proposed memory surface development requires only two extra constitutive parameters (μ and ς) in addition to those required for the selected baseline model, making a total number of 12 necessary parameters. These are summarised and described in Table 1.

Calibration of parameters and their influence on simulations

Parameters of the baseline model

The calibration procedure and the influence of the parameters related to the newly introduced memory surface is presented here with reference to the experimental work performed by Escribano (2014) on Hostun RF sand. The parameters for the baseline soil model (first ten parameters in Table 1, from G to k_d) have been calibrated to obtain satisfactory simulations of the stress ratio-deviatoric strain (η-ε_q) and volumetric trends (ε_v-ε_q), shown in Fig. 4a and Fig. 4b respectively, and the selected parameters well agree with published simulation attempts on similar materials (Diambra et al. 2010, Diambra et al. 2011). These show triaxial drained compression tests on four sand specimens of different densities and tested under conventional drained triaxial test conditions at different constant cell confining pressures. The elastic parameters have been deduced from the empirical relationship proposed by Hardin and Black (1966); the proposed formulation is slightly modified to ensure dimensional consistency:

$$\frac{G_0}{p_{atm}} = 323 \frac{(2.97-e)^2}{1+e} \sqrt{\frac{p}{p_{atm}}} \tag{31}$$

where G_0 is the dynamic shear modulus and p_{atm}=100 kPa represents the atmospheric pressure. The elastic shear modulus is assumed to correspond to the dynamic modulus defined in Eq. (31). It was observed that after many loading cycles, when the soil was in a pseudo-elastic condition, Eq. (31) well described the elastic shear modulus. The critical state parameters υ_λ and λ were selected following the experimental campaign on Hostun Sand of Escribano (2014), while the parameters A, k_d and B were calibrated following the existing guidelines for the calibration of the Severn-Trent Sand model for Hostun Sand (Gajo and Muir Wood, 1999a).

Parameters for memory surface evolution

The available drained cyclic triaxial tests performed by Escribano (2014) consisted of a preliminary shearing under constant mean stress (p) to a target stress ratio η^{ave} from which the cyclic shear stress with amplitude of stress ratio $\Delta\beta=\Delta q/p$ was applied symmetrically, varying only the axial vertical stress and keeping a constant cell pressure, as shown in Fig. 5a-b. For the following simulations, there is a discrepancy between experiments and simulations during the first half-cycle, and for this reason the concept of accumulated strain ε^{acc}, as defined by Wichtmann (2005) is introduced. This represents the permanent strain accumulated during cyclic loading at the end of each cycle.

The constitutive parameter μ controls the evolution of stiffness within the memory surface and governs strain accumulation during cyclic loading. The calibration of μ requires experimental results from cyclic tests. The value of the parameter was chosen by simultaneously and satisfactorily fitting the trend of strain accumulation with the number of cycles shown in Fig. 6a and fitting the stress-strain response during renewed monotonic loading at the end of the cyclic stage, as shown in Fig. 6b.

Fig. 7a-b provides a parametric analysis on the influence of the constitutive parameter μ for the strain accumulation during cyclic loading and the stress-strain response on subsequent monotonic reloading to failure. It is possible to increase the importance of the distance b^M in the definition of the hardening modulus (see Eqs (19) and (20)) by increasing μ resulting in more rapid soil stiffening (Fig. 7b) and thus less accumulation of deviatoric strains with number of cycles (Fig. 7a). Increasing the hardening modulus through μ reduces the overshooting on subsequent monotonic reloading (Fig. 7b) because the surface expansion (which bounds an increased stiffness region) is reduced by the lower plastic permanent volumetric strain developed (see Eq. 24).

421 The contraction term introduced in Eq. (24) is essential for a reasonable prediction of the soil
422 behaviour under undrained cyclic loading conditions. As suggested by experimental evidence
423 (Ishihara et al., 1975, Georgiannou et al., 2008), contraction of the memory surface occurs
424 only when the soil experiences dilative plastic volumetric strains. A comparison of model
425 simulations with and without the damage mechanism is provided in Fig. 8. Without the
426 contraction mechanism, continuous cycling would cause progressive expansion of the
427 memory surface inducing a progressive soil stiffening (Fig. 8a-b). By contrast, the damage
428 rule in Eq. (24) permits rapid contraction of (damage to) the memory surface when the soil
429 experiences plastic dilative strains and allows the correct qualitative simulation of pore water
430 pressure build up and effective stress path response (Fig. 8c-d). Under drained conditions the
431 memory surface progressively contracts leading to a large strain accumulation, and an almost
432 constant accumulated strain rate; this is consistent with the experiments performed by
433 Wichtmann (2005) where it was experimentally observed that for a dense soil cycled at a
434 high average stress ratio soil stiffening is rather slow leading to a large accumulation.
435 The rate of memory surface contraction is governed by the parameter ς in Eq. (24) and its
436 influence on the simulations for loading-unloading undrained triaxial tests with stress reversal
437 is illustrated in Fig. 9. Reducing ς results in an increased rate of contraction of the memory
438 surface which is reflected in Fig. 9 by the reduced extent of the stiffer response zone within
439 the memory surface during the unloading stage. While the influence of this parameter for the
440 drained test conditions simulated in the following is generally negligible, a value of
441 parameter ς=0.00003 was imposed.
442
443

Model simulations and performances

The use of the model to simulate the experimentally observed cyclic drained response of Hostun RF sand at different densities, stress ratios and initial mean pressure (Escribano, 2014) is explored in this section. The single set of constitutive parameters presented in Table 1 has been adopted.

Typical simulations

Typical simulations of the deviatoric stress-strain and volumetric soil behaviour under drained cyclic triaxial loading are shown in Fig. 10 and Fig. 11 for both loose and dense specimens, cycled at constant mean pressure of p=100 kPa but at different average stress ratios, η^{ave} =0.25 and 0.50, respectively. The cyclic amplitude $\Delta\beta$=0.31-0.33 was rather similar for all the four tests simulated. The model simulates the experimental data quite well; the predictions are good for the accumulated deviatoric strains for all the four tests and a smaller accumulation of strains is predicted with increased specimen density (compare Fig. 10a-b and Fig. 11a-b). The trends in the volumetric planes in Fig. 10c-d and Fig. 11c-d are well reproduced with limited influence of the density on the slope of the responses. There are some small discrepancies on the predicted slopes of the accumulated ε_v-ε_q trends, with the modelling suggesting (as expected) a steeper slope for the looser sample. These slopes are indeed governed by the adopted flow rule in Eq.(13).

Rate of accumulation of plastic strains

An explicit comparison of measured and predicted accumulation of deviatoric and volumetric plastic strains with the number of cycles for specimens cycled at different densities and average stress ratios is presented in Fig. 12 and Fig. 13. The tests in Fig. 12 were all cycled at an average stress ratio $\eta^{ave}=0.5$, while the soil density and cell confining pressure are varied.

469 The proposed model generally captures rather well the magnitude of the deviatoric strains
470 and the order of the trends of the different tests (Fig. 12a-b). The magnitude and order of the
471 volumetric trends is also quite well captured but probably with less accuracy, as the model
472 seems to underestimate the volumetric strains for the loosest void ratio e_0=0.819 and slightly
473 overestimate for the densest e_0=0.718 (Fig. 12c-d). Experimental uncertainty may be relevant
474 perhaps induced by non-uniformities of volumetric strains that may occur during cycling
475 (Escribano, 2014) or there may be an effect of isotropic testing stress level (p_0) which is not
476 fully captured by the proposed memory surface expandion rule. The tests in Fig. 13 were all
477 performed on loose specimens (relative densities D_r=7% to 29%) at the same confining
478 pressure but with different average stress ratio η^{ave} =0, 0.25 and 0.50. The model simulates
479 the deviatoric responses and even predicts negative deviatoric strains when cyclic loading is
480 applied at η^{ave}=0 (Fig. 13a-b). There is also a good agreement between measured
481 accumulated volumetric strains (Fig. 13c) and related model predictions (Fig. 13d) except for
482 the test in which cyclic loading is applied at η^{ave}=0, where the model underestimates
483 volumetric accumulated strains. This discrepancy at low average stress ratio stress states may
484 be linked to the adopted flow rule (Eq. (13)) and the employment of a non-linear dilatancy
485 function (e.g. Li and Dafalias 2000, Cazacliu and Ibraim 2016; Ibraim et al. 2010) may lead
486 to more accurate predictions.
487 *Cyclic tests with variable amplitude*
488 In a more realistic scenario, soil is subjected to cyclic amplitudes of different magnitudes.
489 Such conditions have been reproduced in the triaxial cell, where a sample of medium density
490 (e_0=0.925 and p_0=100 kPa) was subjected to cyclic amplitude of different magnitudes. The
491 test was performed following the loading stages shown in Fig. 14. The target average stress
492 ratio, at which cyclic loading was applied, was always reached through shearing the sample at
493 constant mean pressure (stages AB, BD, DF and FH in Fig. 14), with η^B=0.2, η^D=0.5, η^F=0.7

494 and η^H=0.9. The cyclic loading was then applied under typical triaxial conditions (stages BC,
495 DE, FG and HI in Fig. 14) imposing $\Delta\beta^{BC}$=0.18 for N_{cyc}=50, $\Delta\beta^{DE}$=0.48 for N_{cyc}=5,
496 $\Delta\beta^{FG}$=0.62 for N_{cyc}=10 and $\Delta\beta^{HI}$=0.84 for N_{cyc}=10. The sample was finally subjected to
497 monotonic shearing at constant mean pressure. The comparison between the experimental
498 findings and model predictions is shown in Fig. 15a-b-c-d. The experimental stress-strain
499 response (Fig. 15a) is well reproduced by the model as shown in (Fig. 15b) even though the
500 response from model simulations seems to be stiffer than the predicted one. The model
501 predicted just elastic response while simulating the first cyclic sequence (BC) because the
502 stress state was always enclosed within the elastic region. The measured volumetric strains
503 (Fig. 15c) are generally lower than the predicted ones (Fig. 15d). Experimentally, soil seems
504 to dilate during the first cyclic loading sequence (Fig. 15c) while just pure contraction would
505 be expected. These discrepancies might be related with non-uniformities in the experimental
506 measurements of volumetric strains.
507
508 **Conclusions**
509 This paper proposes additional ingredients for kinematic hardening bounding surface
510 constitutive models to improve the simulation of the behaviour of granular soils under large
511 number of repeated/cyclic loading. The proposed formulation incorporates an additional
512 memory surface, which represents the somewhat stable fabric associated with the historic
513 stress states which the soil has the feeling that it has already experienced. When the stress
514 state lies inside the memory surface, an additional hardening term depending on the distance
515 of the current stress state to the memory surface is introduced to capture the stiffer soil
516 behaviour typically observed during repeated loading by comparison with virgin loading.
517 The memory surface evolves according to three rules each of which can be linked
518 qualitatively to the changes in fabric (particle arrangement) which result from the occurrence

519 of plastic strains and which tend to modify the ability of the soil to remember its past. Rule 1)
520 The memory surface changes in size following the experienced plastic strains. Rule 2) The
521 memory surface always encloses the current stress state. Rule 3) The memory surface always
522 encloses the current yield surface. The expansion of the memory surface with plastic
523 contractive volumetric strains is the key development which permits successful simulation of
524 the stiffening behaviour of soil under cyclic loading conditions and also the increased stress
525 range for stiff response observed upon monotonic reloading following a series of cyclic stress
526 changes.
527 Evidently, such a modelling framework can be constructed using any desired elasto-plastic
528 constitutive model as the basic element. Just two additional constitutive parameters are
529 needed. The value of the proposed modelling framework has been demonstrated against an
530 extensive testing campaign of drained cyclic triaxial tests on Hostun RF sand. Accuracy of
531 prediction of accumulated deviatoric and volumetric strain has been shown for tests on
532 samples with a range of initial density, up to 1500 loading cycles of different amplitude and
533 average stress ratio.
534 Though the model has been formulated in terms of stress and strain conditions which are
535 accessible in the axisymmetric triaxial apparatus, the memory surface concept and its
536 hardening mechanisms have been described qualitatively in a general principal stress.
537 There are improvements to the model that might be anticipated. These might include:
538 modifications to the detail of the functions and criteria which govern the expansion and
539 translation of the memory surface; a closer inspection of the behaviour of the soil under
540 cycles of loading which incur plastic volumetric expansion – noting that such volume
541 changes tend to be linked with shearing at high stress ratios for which localisation and other
542 undesirable responses may occur which may undermine the reliability of experimental data –
543 and the inclusion of an anisotropic elastic stiffness matrix which is more sensitive to the

plastic strains that have occurred (which themselves indicate changes in soil fabric through particle slippage and rearrangement). However, the emphasis in the model development has been on the minimum degree of complexity required to describe features of response which are observed experimentally.

Acknowledgments

The authors are grateful to the Queen's School of Engineering of the University of Bristol that offered financial support to this work.

Notation list

The following symbols are used in the paper:

A = flow rule multiplier;

B = monotonic loading hardening modulus constitutive parameter;

b = distance between the stress state and its image on the bounding surface;

b^M = distance between the stress state and its image on the memory surface;

b_{max} = maximum value of b;

b^M_{max} = maximum value of b^M;

d = dilatancy;

$\boldsymbol{D}^e$ = elastic stiffness matrix ($\overline{\boldsymbol{D}}^e$ in the normalised stress space);

$\boldsymbol{D}^{ep}$ = elasto-plastic stiffness matrix;

e_0= initial void ratio;

f = yield function;

F = bounding surface function;

f^M = memory surface function;

569 G = elastic shear modulus;

570 H = hardening modulus;

571 H^M = hardening modulus if stress state $\bar{\boldsymbol{\sigma}}$ coincides to the image stress on the memory

572 surface $\bar{\boldsymbol{\sigma}}^M$;

573 k = effect of state parameter on soil strength constitutive parameter;

574 K = elastic bulk modulus;

575 k_d = flow rule constitutive parameter;

576 M_{cs} = critical state line slope; M_{cv} and M_{ev} in compression and extension, respectively;

577 $\boldsymbol{m}$ = unit direction of plastic flow $\boldsymbol{m}=[m_q, m_p]^{\mathrm{T}}$; $\boldsymbol{m}^*$ is its transformation in the normalised

578 stress space;

579 m = yield surface opening; $m=m_c$ or m_e in compression and extension, respectively;

580 m^M = memory surface opening; $m^M=m_c^M$ or m_e^M in compression and extension, respectively;

581 $\boldsymbol{n}$ = unit loading direction $\boldsymbol{n}=[n_q, n_p]^{\mathrm{T}}$;

582 p = effective mean pressure (p_0 initial mean pressure);

583 p_{atm} = 100 kPa, atmospheric pressure;

584 q = deviatoric stress;

585 R = ratio of opening of yield surface and strength surface;

586 t = quantity to distinguish between compression (t=1) and extension (t=-1);

587 $z=|M_{cs}|/(M_{cv}+|M_{ev}|)$;

588 $\boldsymbol{\alpha}$ = yield surface centre $\boldsymbol{\alpha}=[\alpha_q, \alpha_p]^{\mathrm{T}}$. The slope is calculated as $\alpha=\alpha_q/\alpha_p$;

589 $\boldsymbol{\alpha}^M$ = memory surface centre $\boldsymbol{\alpha}^M=[\alpha^M{}_q, \alpha^M{}_p]^{\mathrm{T}}$.The slope is calculated as $\alpha^M=\alpha^M{}_q/\alpha^M{}_p$;

590 $\Delta\beta$ = cyclic amplitude ($=\Delta q/p_0$);

591 $\delta\boldsymbol{\varepsilon}$ = strain increment vector; $\delta\varepsilon_q$ and $\delta\varepsilon_v$ deviatoric and volumetric strain increment;

592 $\delta\varepsilon^p{}_v$ = plastic volumetric strain increment;

593 ε_v^{acc} = accumulated volumetric strains;

ε_q^{acc} = accumulated deviatoric strains;

$\bar{\eta}$ = normalised stress ratio;

$\bar{\eta}^M$ = stress ratio for $\bar{\boldsymbol{\sigma}}^M$;

η^{ave} = cyclic average stress ratio;

λ = critical state line slope in υ-ln p plane;

μ = memory surface hardening modulus constitutive parameter;

ν = Poisson's ratio;

$\boldsymbol{\sigma}$ = current stress state;

$\bar{\boldsymbol{\sigma}}$ = normalised stress state;

$\bar{\boldsymbol{\sigma}}^B, \bar{\boldsymbol{\sigma}}^M$ = image stresses on the bounding surface and memory surface;

ς = memory surface damage constitutive parameter;

τ = scalar quantity to calculate $\delta\boldsymbol{\alpha}$;

υ = specific volume;

υ_λ = intercept for critical state line in the υ-ln p plane;

ϕ_{cv} = critical state friction angle.

References

Al-Tabbaa, A. and Muir Wood, D. (1989). "An experimentally based "bubble" model for clay." *NUMOG III*, Niagara Falls, Canada.

Argyris, J. H. F., G., Szimmat, J., Warnke, E. P. and William, K.J. (1974). "Recent developments in the finite element analysis of prestressed concrete reactor vessels." *Nucl. Eng. and Des.*, 28(1), 42-75.

Been, K. and Jefferies, M. (1985). "A state parameter for sands." *Géotechnique*, 35(1), 99-112.

618 Cazacliu, B., Ibraim, E. (2016). “Elasto-plastic model for sand including time effect.”
619 *Géotechnique Letters*, 6(1), 16-22 (DOI: 10.1680/jgele.15.00106)
620 Chow, S.H., O’Loughlin, C.D., Corti, R., Gaudin, C. and Diambra A. (2015). “Drained cyclic
621 capacity of plate anchors in dense sand: Experimental and theoretical observations.”
622 *Géotechnique Letters*, 5(Q2), 80-85.
623 Corti, R., Diambra, A., Nash, D.F.T., & Muir Wood, D. (2015) “An evolving memory
624 surface for modelling the cyclic behaviour of granular soils” *Proceedings of the XV Pan-*
625 *American Conference on Soil Mechanics and Geotechnical Engineering*, Buenos Aires,
626 Argentina.
627 Dafalias, Y. F. and Manzari, M. T. (2004). “Simple plasticity model accounting for fabric
628 change effects.” *J. Eng. Mech.,* 10.1061/(ASCE)0733-9399(2004)130:6(622), 622-634.
629 Di Benedetto, H., Blanc, M., Tiouajni, S. and Ezaoui, A. (2014). “Elastoplastic model with
630 loading memory surface (LMS) for monotonic and cyclic behaviour of geomaterials.” *Int. J.*
631 *Numer. Anal. Methods Geomech.,* 38(14), 1477-1502.
632 Diambra, A., Ibraim, E., Wood, D. M., and Russell, A. R. (2010). “Fibre reinforced sands:
633 Experiments and modelling.” *Geotext. Geomembranes*, 28(3), 238-250.
634 Diambra, A., Ibraim, E., Russell, A. R., and Wood, D. M. (2011). “Modelling the undrained
635 response of fibre reinforced sands.” *Soils and Found.*, 51(4), 625-636.
636 Diambra, A., Ciavaglia, F., Harman, A., Dimelow, C., Carey, J., and Nash, D. F. T. (2014).
637 “Performance of cyclic cone penetration tests in chalk.” *Géotechnique Letters*, 4(Q3), 230-
638 237.
639 Escribano, D. E. (2014). “Evolution of stiffness and deformation of Hostun Sand under
640 drained cyclic loading.” Ph.D. thesis, Univ. of Bristol, UK.
641 Gajo, A. and Muir Wood, D. (1999a). “Severn-Trent sand: a kinematic-hardening constitutive
642 model: the *q-p* formulation.” *Géotechnique*, 49(5), 595-614.

643 Gajo, A. and Muir Wood, D. (1999b). "A kinematic hardening constitutive model for sands:
644 the multiaxial formulation." *Int. J. Numer. Anal. Methods Geomech.*, 23(9), 925-965.
645 Georgiannou, V. N., Tsomokos, A. and Stavrou, K. (2008). "Monotonic and cyclic behaviour
646 of sand under torsional loading." *Géotechnique*, 58(2), 113-124.
647 Hardin, B. O. and Black, W. L. (1966). "Sand stiffness under various triaxial stresses."
648 *Journal of the Soil Mechanics and Foundations Division*, 92(2), 27-42.
649 Ibraim, E., Lanier, J., Muir Wood, D. and Viggiani, G., (2010). "Strain path controlled shear
650 tests on an analogue granular material." *Géotechnique* 60 (7), 545–559 (DOI:
651 10.1680/geot.8.P.100).
652 Ishihara, K., Tatsuoka, F. and Yasuda, S. (1975). "Undrained Deformation and Liquefaction
653 of Sand Under Cyclic Stresses." *Soils and Found.*, 15(1), 29-44.
654 Jafarzadeh, F., Javaheri, H., Sadek, T. and Muir Wood, D. (2008). "Simulation of anisotropic
655 deviatoric response of Hostun sand in true triaxial tests." *Comput. and Geotech.*, 35(5), 703-
656 718.
657 Klinkvort, R. T. and Hededal, O. (2013). "Lateral response of monopile supporting an
658 offshore wind turbine." *P. I. Eng-Geotech.*, 166(2), 147-158.
659 Leblanc, C., Houlsby, G. T. and Byrne, B. W. (2009). "Response of stiff piles in sand to
660 long-term cyclic lateral loading." *Géotechnique*, 60(2), 79-90.
661 Li, X.S. and Dafalias, Y.F. (2000) "Dilatancy for cohesionless soils." *Géotechnique*, 50(4),
662 449-460.
663 Manzari, M. T. and Dafalias, Y. F. (1997). "A critical state two-surface plasticity model for
664 sands." *Géotechnique*, 47(2), 255-272.
665 Maleki, M., Cambou, B. and Dubujet, P. (2009). "Development in modelling cyclic loading
666 of sands based on kinematic hardening." *Int. J. Numer. Anal. Methods Geomech.*, 33(14),
667 1641-1658.

668 McVay, A. M. and Taesiri, M. (1985). “Cyclic behaviour of pavement base materials.” *J.*
669 *Geotech. Eng.*-ASCE, 10.1061/(ASCE)0733-9410(1985)111:1(1), 1-17.
670 Mroz, Z. (1967). “On the description of anisotropic work hardening.” *J. Mech. Phys. Solids*,
671 15(3), 163-175.
672 Mroz, Z., Norris, V. A. and Zienkiewicz, O. C. (1978). “An anisotropic hardening model for
673 soils and its application to cyclic loading.” *Int. J. Numer. Anal. Methods Geomech.,* 2(3),
674 203-221.
675 O'Sullivan, C. and Cui, L. (2009). “Micromechanics of granular material response during
676 load reversals: Combined DEM and experimental study.” *Powder Technol.*, 193(3), 289-302.
677 Papadimitriou, A. G., Bouckovalas, G. D. and Dafalias, Y. F. (2001). “Plasticity model for
678 sand under small and large cyclic strains.” *J. Geotech. Geoenviron. Eng.,*
679 10.1061/(ASCE)1090-0241(2001)127:11(973), 973-983.
680 Papadimitriou, A. G. and Bouckovalas, G. D. (2002). “Plasticity model for sand under small
681 and large cyclic strains: a multiaxial formulation.” *Soil Dyn. Earthq. Eng.*, 22(3), 191-204.
682 Randolph, M. and Gourvenec, S. (2011). *Offshore Geotechnical Engineering*, Spon Press,
683 New York, NY.
684 Stallebrass, S. E. and Taylor, R. N. (1997). “The development and evaluation of a
685 constitutive model for the prediction of ground movements in overconsolidated clay.”
686 *Géotechnique*, 47(2), 235-253.
687 Tatsuoka, F., Jardine, R., Lo Presti, D., Di Benedetto, H. and Kodaka, T. (1997). “Theme
688 Lecture: Characterising the pre-failure deformation properties of geomaterials.” *Proc., XIV*
689 *Int. Conf. on Soil Mechanics and Foundation Engineering 4*, Hamburg, 2129-2164.
690 Wichtmann, T. (2005). “Explicit accumulation model for non-cohesive soils under cyclic
691 loading.” Ph.D. thesis, Bochum Ruhr- Univ., Germany.

692 Wichtmann, T., Niemunis, A. and Triantafyllidis, T. (2005). “Strain accumulation in sand due
693 to cyclic loading: drained triaxial tests.” *Soil Dyn. Earthq. Eng.,* 25(12), 967-979.
694 Yu, H.S. (2006). “Multi-surface and bounding surface plasticity.” *Plasticity and geotechnics*
695 153-196. Springer US, New York, NY.
696
697 **List of figures**
698 Fig. 1. a) Schematic illustration of the conceptual framework in the triaxial stress plane b)
699 stress-strain response under drained cyclic loading conditions and c) schematic illustration of
700 the framework in the deviatoric stress plane.
701 Fig. 2: Memory surface expansion a) triaxial stress space b) deviatoric stress space; memory
702 surface contraction c) triaxial stress space d) deviatoric stress space.
703 Fig. 3. Representation of the different components of the memory surface model: the memory
704 surface openings m_c^M and m_e^M, and the distances between the current stress state and the
705 image stress points a) triaxial stress plane b) deviatoric stress space.
706 Fig. 4. Calibration of the memory surface model on available drained monotonic triaxial tests
707 (Escribano, 2014) a) stress ratio against deviatoric strain b) volumetric response.
708 Fig. 5. Schematic illustration of a) stress path during experimental cyclic tests b) deviatoric
709 stress variation with number of cycles.
710 Fig. 6. Model calibration a) accumulated deviatoric strains with number of cycles (N_{cyc}=1500)
711 b) stress-strain response with monotonic shearing after 1500 cycles (e_0=0.937, p_0=100 kPa,
712 η^{ave}=0.50 and $\Delta\beta$=0.36).
713 Fig. 7: Effect of variation of the constitutive parameter μ a) accumulated deviatoric strains
714 with the number of cycles b) stress strain response.

715 Fig. 8. Memory surface model simulations (a, b) without the contraction mechanism
716 implemented a) q-p b) q-ε_q and (c, d) including the contraction mechanism c) q-p d) q-ε_q
717 (e_0=0.700, p_0=100 kPa, η^{ave}=0 and $\Delta\beta$=0.64).
718 Fig. 9. Parametric analysis of the damage constitutive parameter ς. 0 – initial state; 1 – stress
719 reversal point; 2a 2b 2c end of the simulation (e_0=0.7 and p_0=100 kPa).
720 Fig. 10. Effect of soil density during drained cyclic loading a) experimental stress-strain
721 curve b) stress-strain curve from simulations c) experimental volumetric response b)
722 volumetric response from simulation (p_0=100 kPa, η^{ave}=0.25, $\Delta\beta$=0.31-0.33).
723 Fig. 11. Effect of soil density during drained cyclic loading a) experimental stress-strain
724 curve b) stress-strain curve from simulations c) experimental volumetric response d)
725 volumetric response from simulations (p_0=100 kPa, η^{ave}=0.50, $\Delta\beta$=0.34-0.36).
726 Fig. 12. Progressive strain accumulation with the number of cycles for dense samples a)
727 experimental deviatoric strain accumulation b) simulation of deviatoric strain accumulations
728 c) experimental volumetric strain accumulation d) simulation of volumetric strain
729 accumulations ($\Delta\beta$=0.33-0.47).
730 Fig. 13. Progressive strain accumulation with the number of cycles for loose samples a)
731 experimental deviatoric strain accumulation b) simulation of deviatoric strain accumulations
732 c) experimental volumetric strain accumulation d) simulation of volumetric strain
733 accumulations ($\Delta\beta$=0.31-0.35).
734 Fig. 14: Schematic representation of the stress path adopted in the test performed at different
735 cyclic amplitudes. Testing conditions: e_0=0.824 and p_0=100 kPa with η^B=0.2, η^D=0.5, η^F=0.7
736 and η^H=0.9. Monotonic loading applied in the stages AB, BD, DF and FH and cyclic loading
737 applied in the stages BC, DE, FG and FI imposing $\Delta\beta^{BC}$=0.18 for N_{cyc}=50, $\Delta\beta^{DE}$=0.48 for
738 N_{cyc}=5, $\Delta\beta^{FG}$=0.62 for N_{cyc}=10 and $\Delta\beta^{HI}$=0.84 for N_{cyc}=10.

739 Fig. 15: Soil response while subjected to varying cyclic amplitude at different average stress
740 ratios a) experimental stress strain response b) stress strain response from simulation c)
741 experimental volumetric response and related d) simulation.
742
743 **List of tables**
744 Table 1: Constitutive parameters of the proposed Memory Surface Hardening Model
745
746

Parameter	Description	Value
G	Elastic Shear Modulus	G_0
v	Poisson's ratio	0.1
ϕ_{cv}	Friction angle at critical state conditions	29.5°
λ	Slope of the critical state line in the v-ln p plane	0.031
υ_λ	Value of the specific volume on the critical state line at p=1 kPa	2.065
R	Ratio between the opening of the yield surface and the strength surface	0.075
B	Parameter controlling hardening modulus	0.0013
k	Parameter controlling the relationship between soil strength and state parameter	3.8
A	Flow rule multiplier	1.1
k_d	State parameter dependence in the flow rule	1.3
μ	New hardening constitutive parameter	16
ς	Damage rule parameter	0.00003

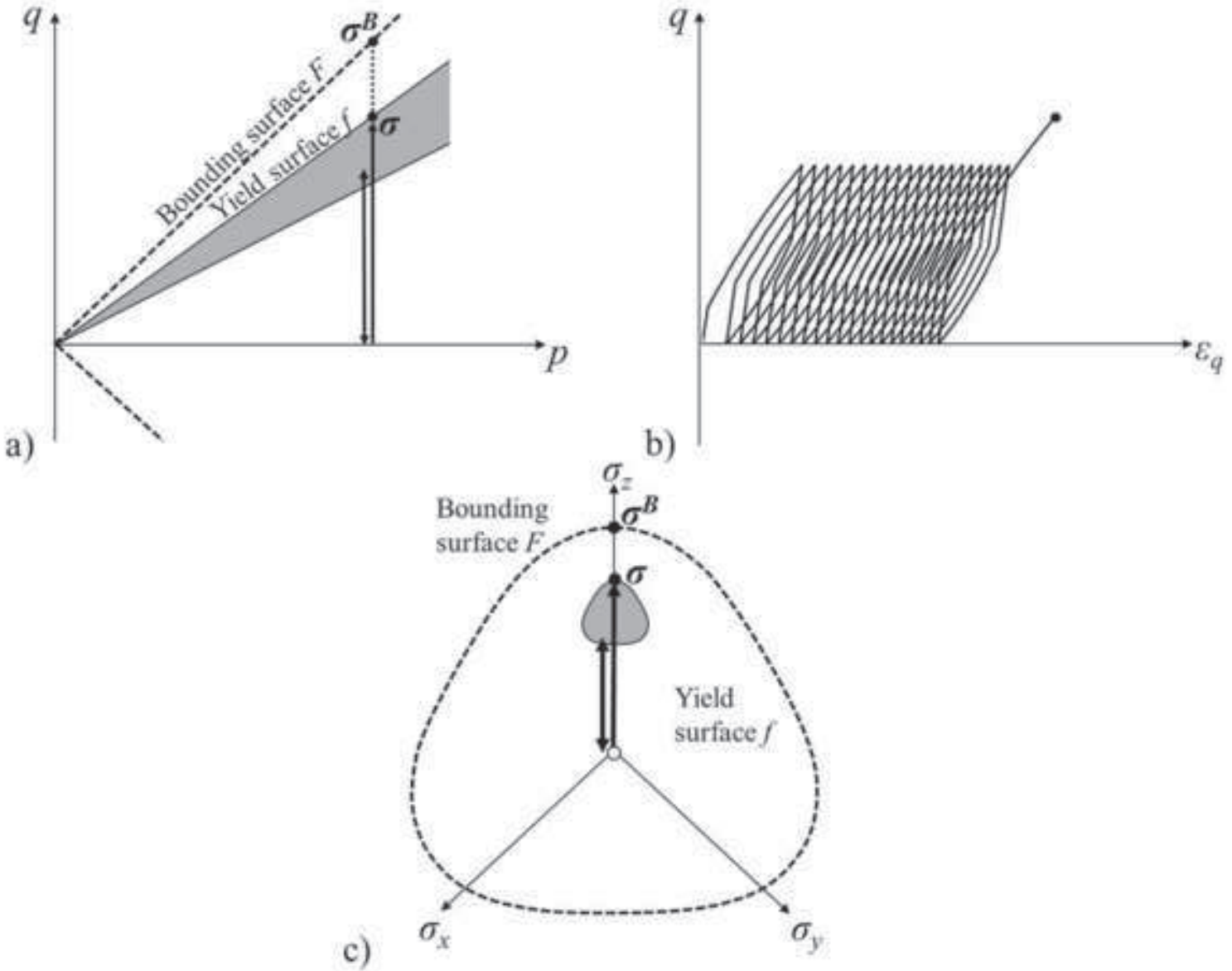

Fig. 1. a) Schematic illustration of the conceptual framework in the triaxial stress plane b) stress-strain response under drained cyclic loading conditions and c) schematic illustration of the framework in the deviatoric stress plane.

Figure

Click here to download Figure Figure 2.tif

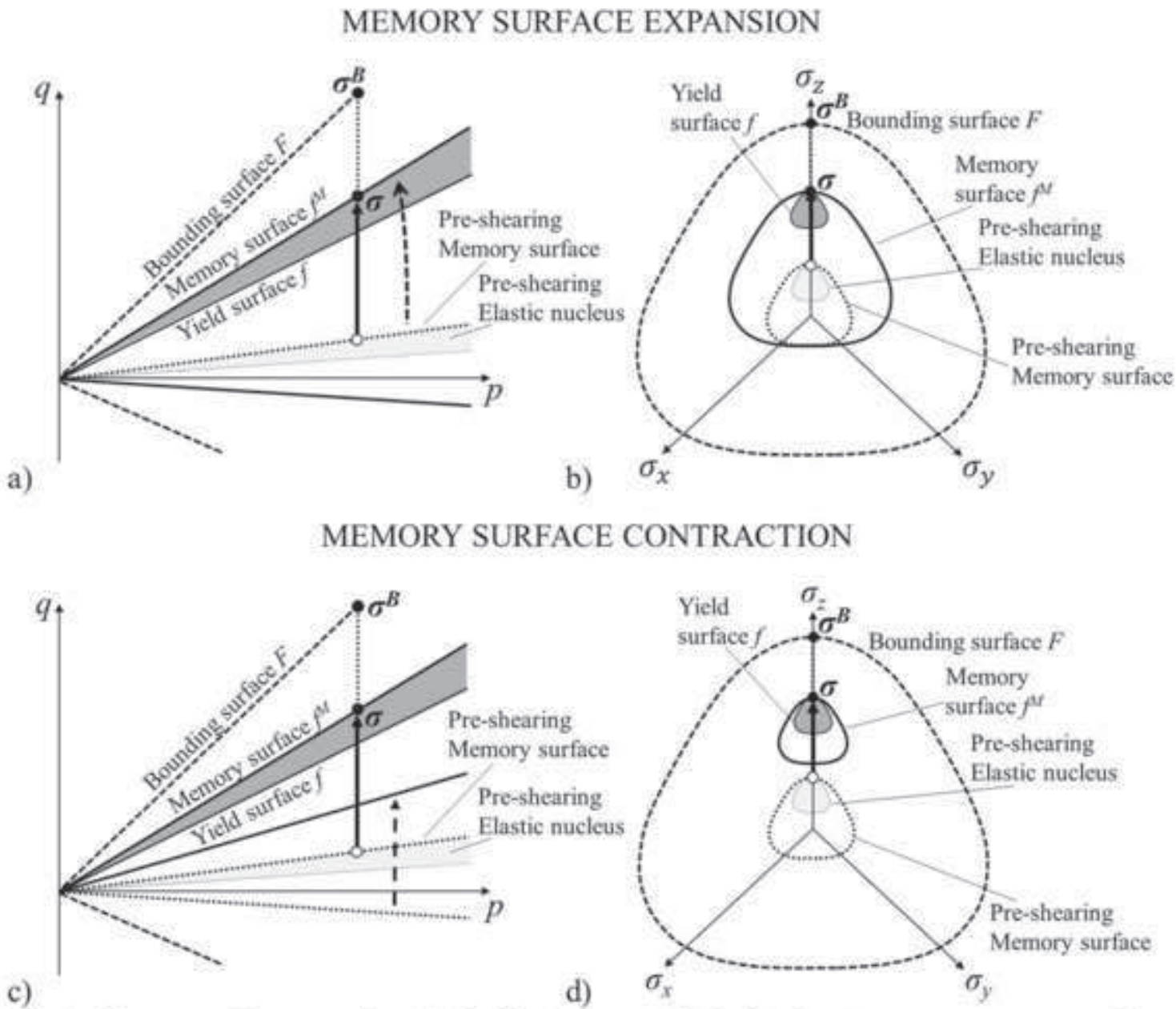

Fig. 2: Memory surface expansion a) triaxial stress space b) deviatoric stress space; memory surface contraction c) triaxial stress space d) deviatoric stress space.

Figure

Click here to download Figure Figure 3.tif

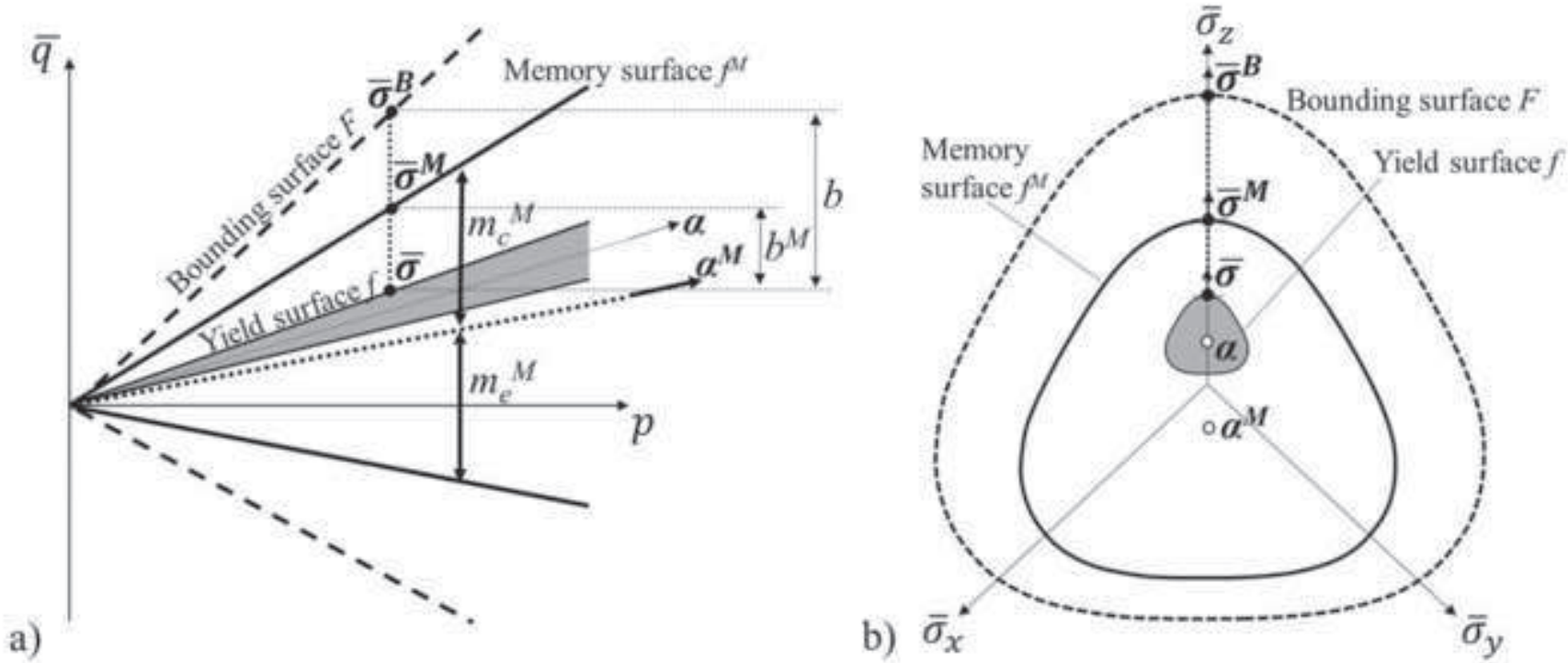

Fig. 3. Representation of the different components of the memory surface model: the memory surface openings m_c^M and m_e^M, and the distances between the current stress state and the image stress points a) triaxial stress plane b) deviatoric stress space.

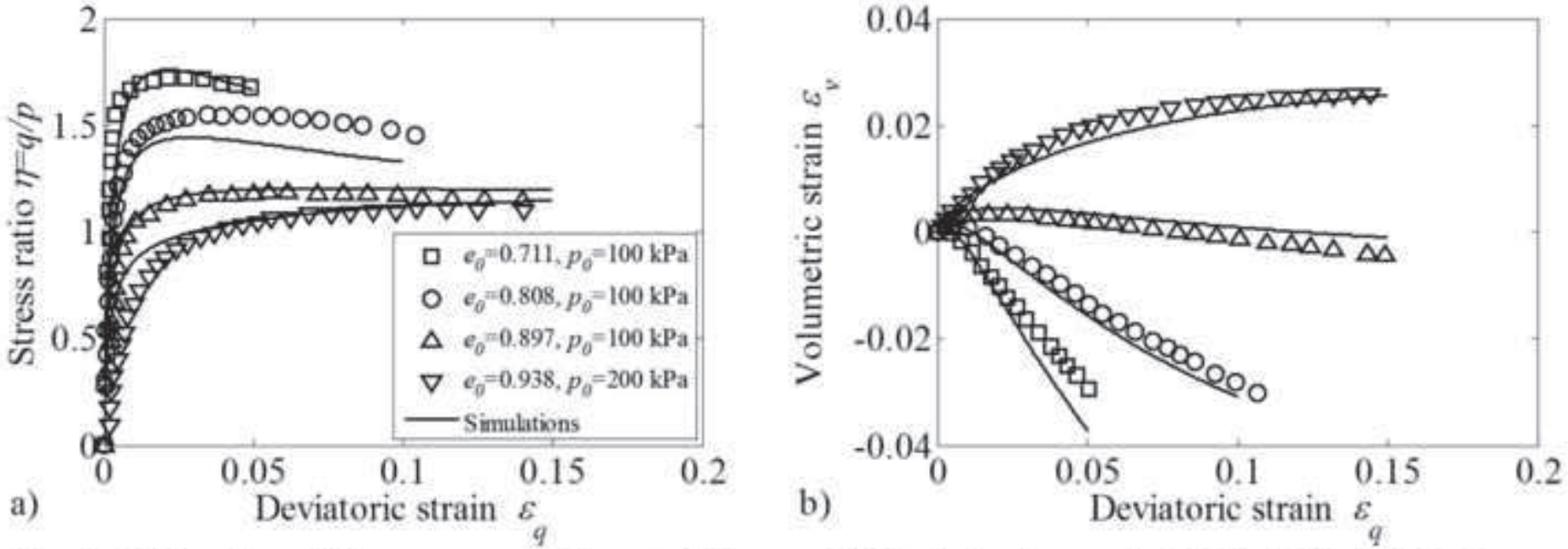

Fig. 4. Calibration of the memory surface model on available drained monotonic triaxial tests (Escribano, 2014) a) stress ratio against deviatoric strain b) volumetric response.

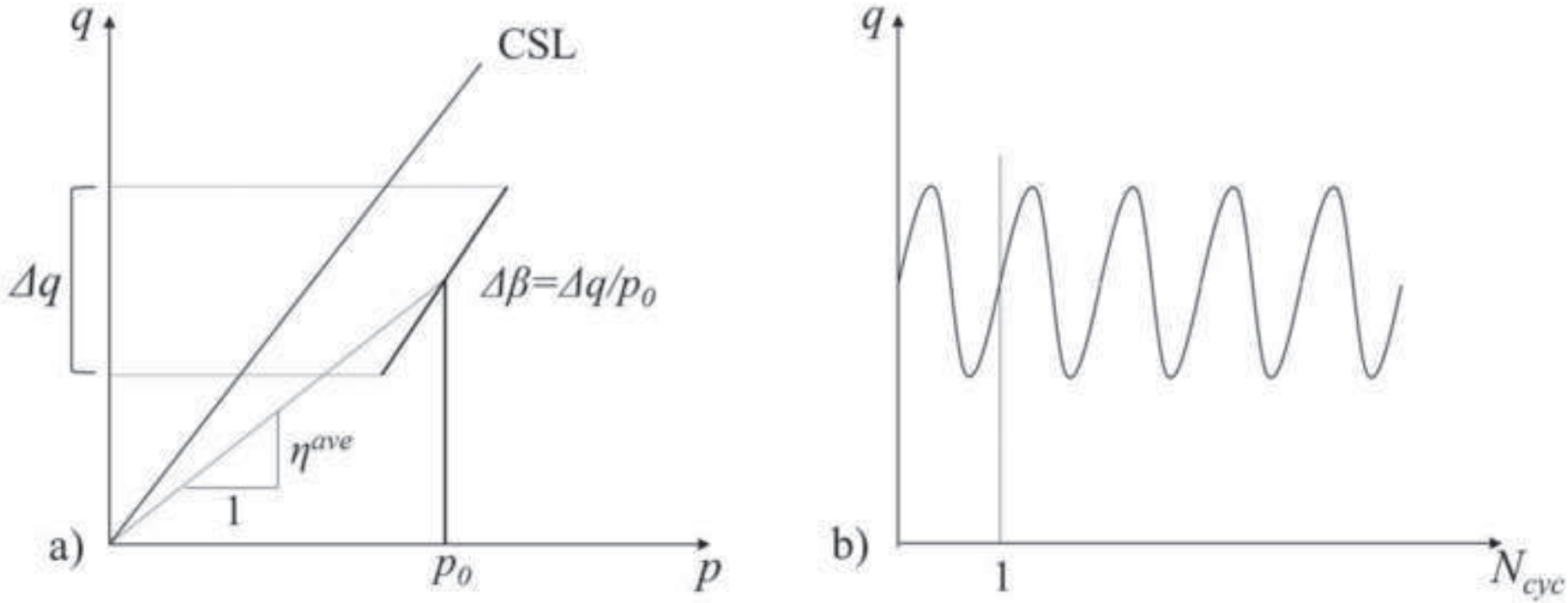

Fig. 5. Schematic illustration of a) stress path during experimental cyclic tests b) deviatoric stress variation with number of cycles.

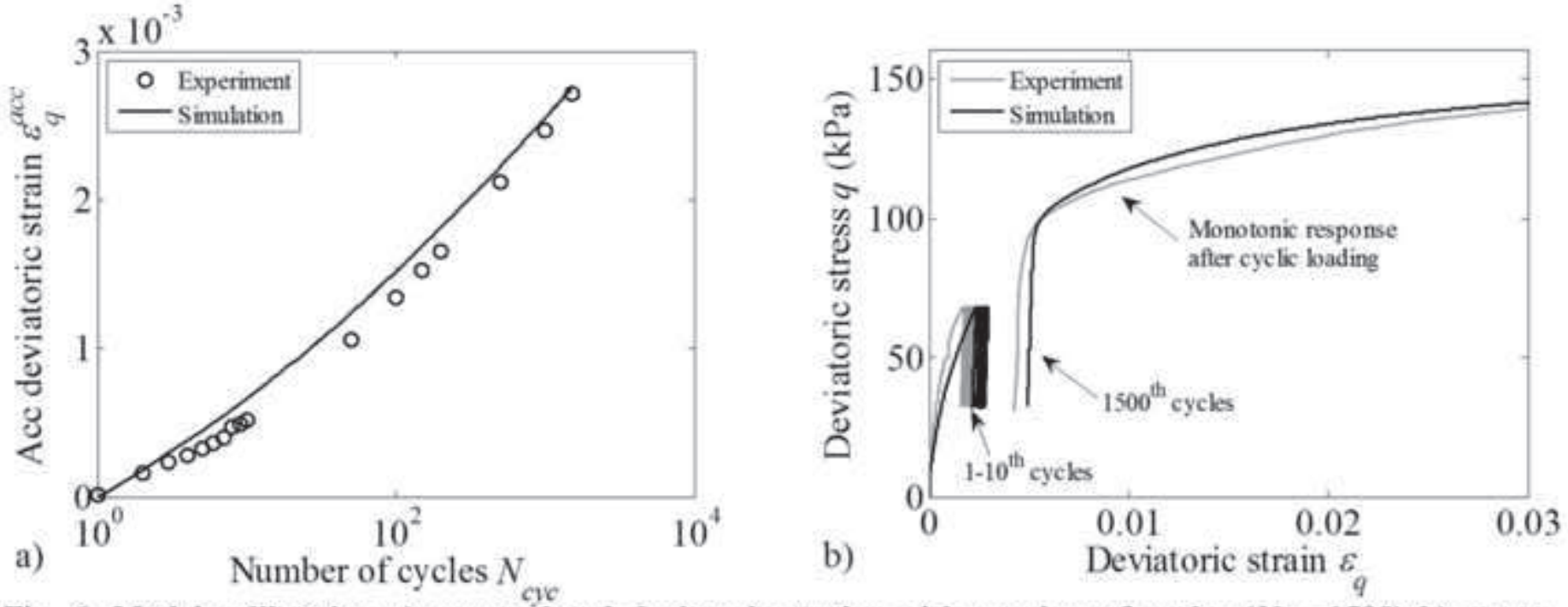

Fig. 6. Model calibration a) accumulated deviatoric strains with number of cycles (N_{cyc}=1500) b) stress-strain response with monotonic shearing after 1500 cycles (e_0=0.937, p_0=100 kPa, η^{ave}=0.50 and $\Delta\beta$=0.36).

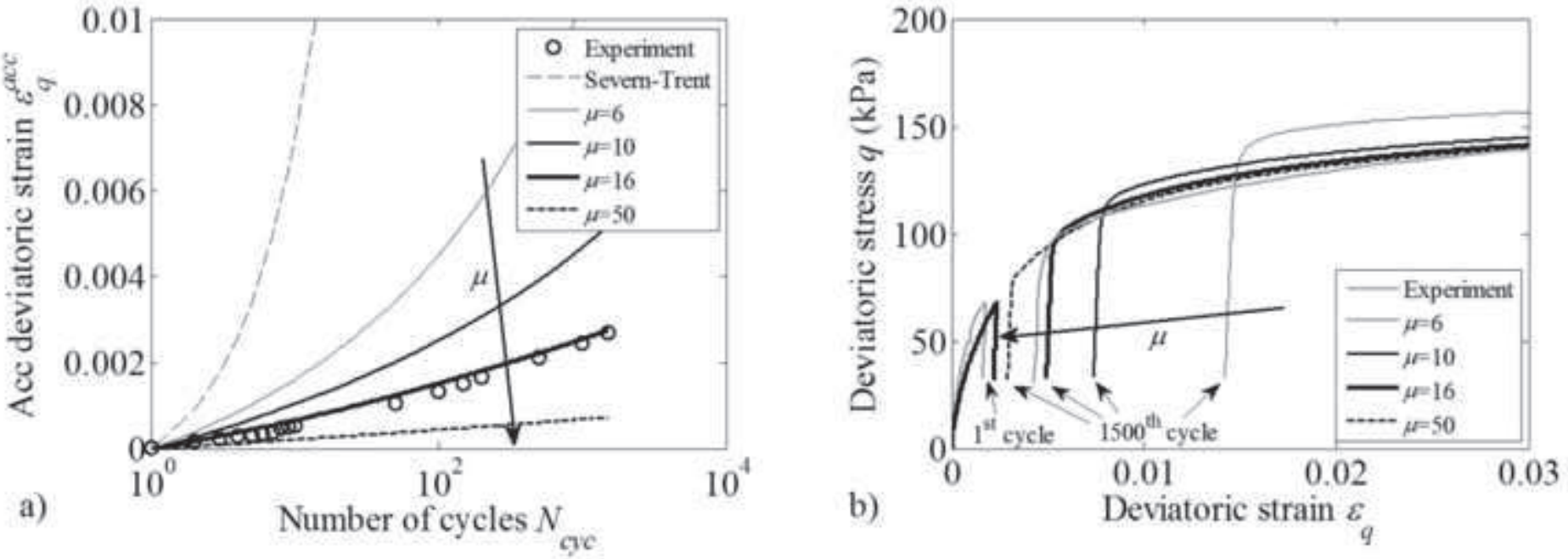

Fig. 7: Effect of variation of the constitutive parameter μ a) accumulated deviatoric strains with the number of cycles b) stress strain response.

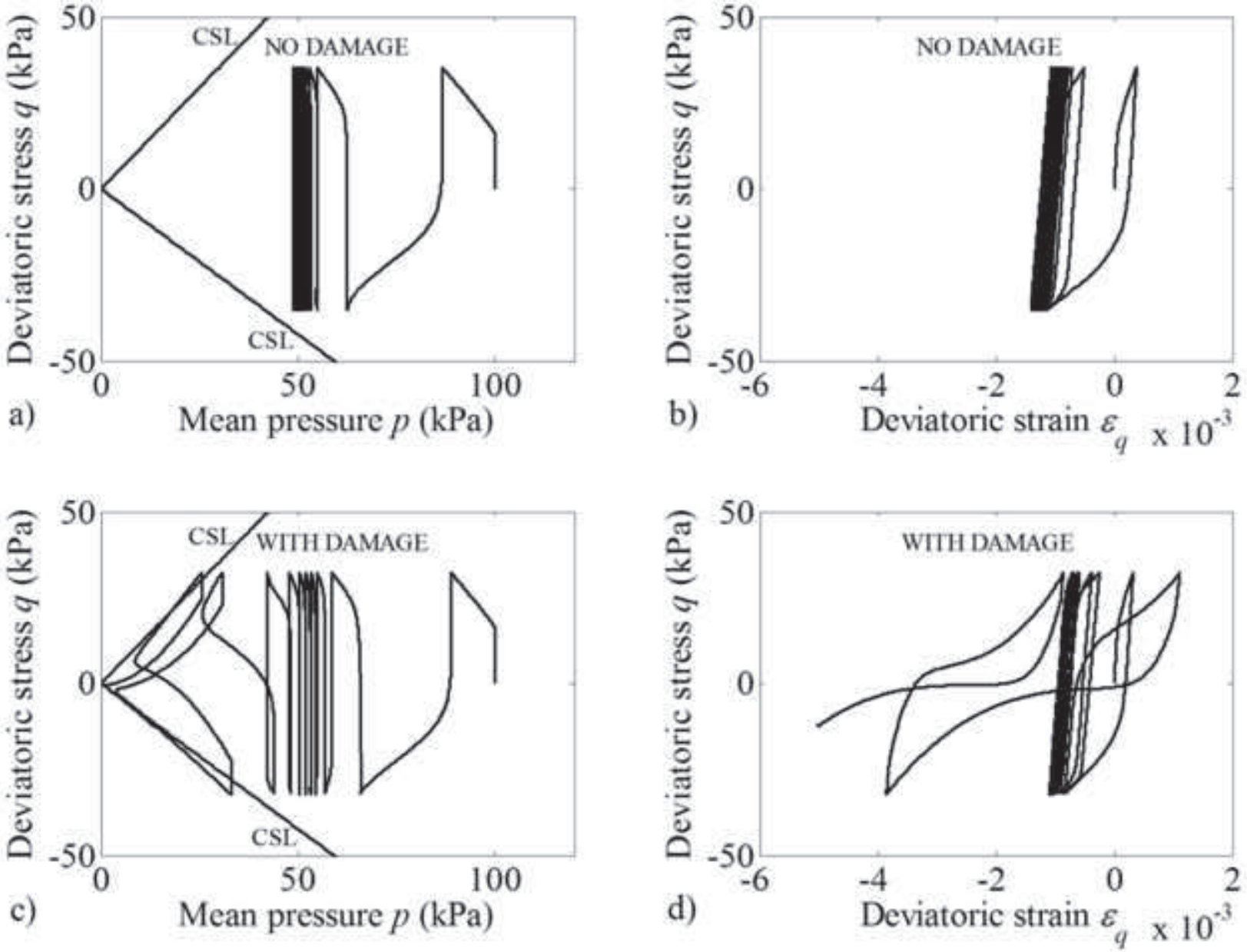

Fig. 8. Memory surface model simulations (a, b) without the contraction mechanism implemented a) q-p b) q-ε_q and (c, d) including the contraction mechanism c) q-p d) q-ε_q (e_0=0.700, p_0=100 kPa, η^{ave}=0 and $\Delta\beta$=0.64).

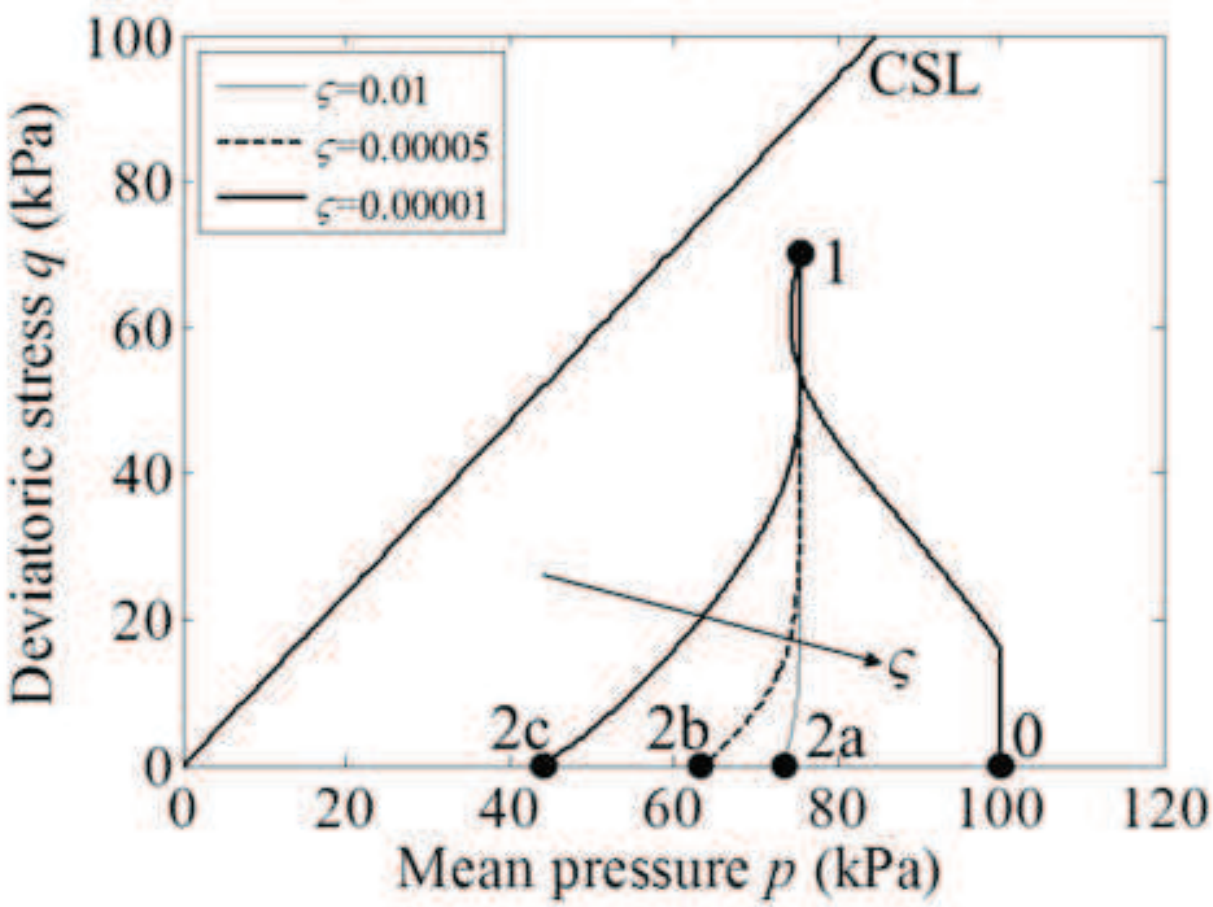

Fig. 9. Parametric analysis of the damage constitutive parameter ς. 0 – initial state; 1 – stress reversal point; 2a 2b 2c end of the simulation (e_0=0.7 and p_0=100 kPa).

Figure

Click here to download Figure Figure 10.tif

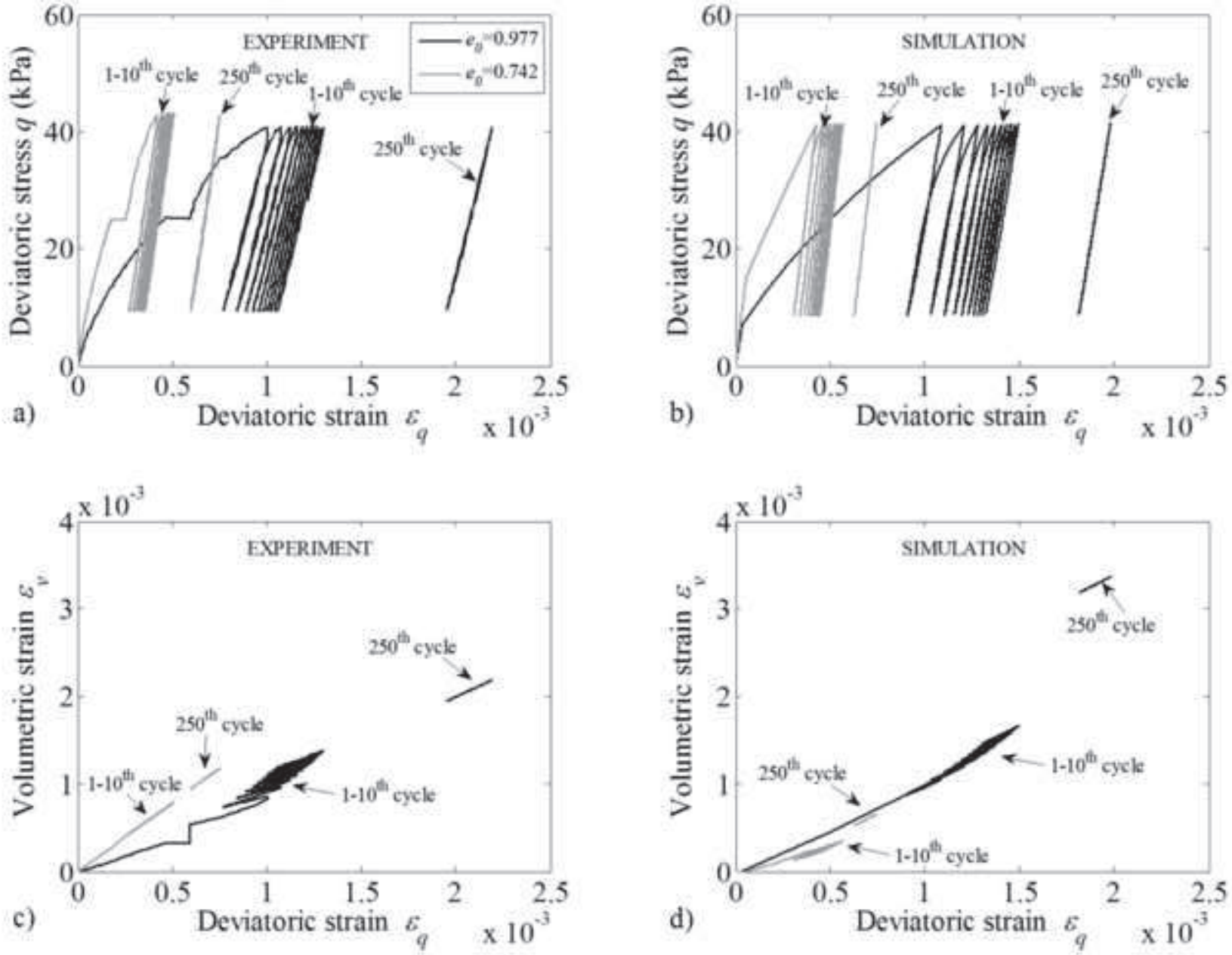

Fig. 10. Effect of soil density during drained cyclic loading a) experimental stress-strain curve b) stress-strain curve from simulations c) experimental volumetric response b) volumetric response from simulation (p_0=100 kPa, η^{ave}=0.25, $\Delta\beta$=0.31-0.33).

Figure

Click here to download Figure Figure 11.tif

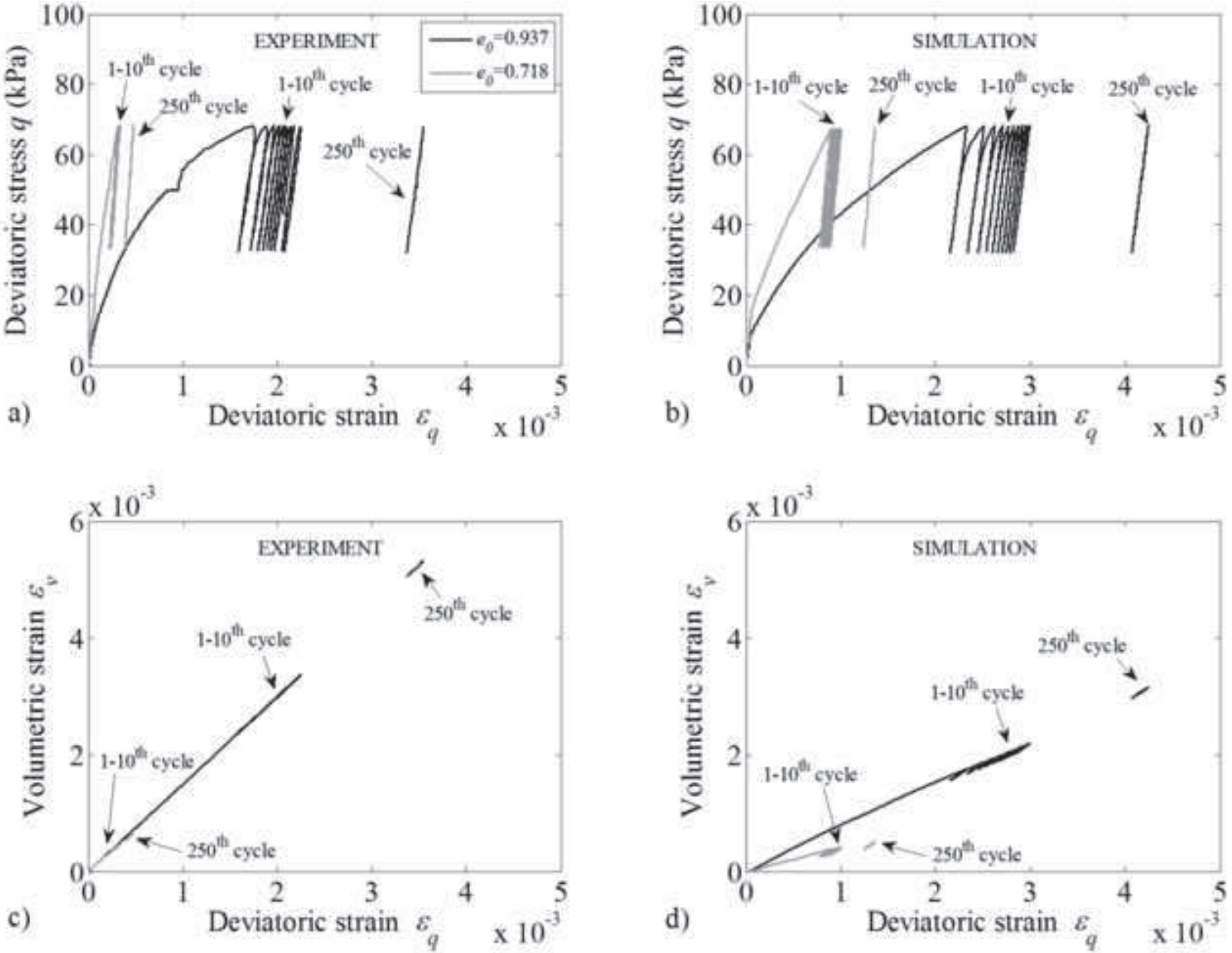

Fig. 11. Effect of soil density during drained cyclic loading a) experimental stress-strain curve b) stress-strain curve from simulations c) experimental volumetric response d) volumetric response from simulations (p_0=100 kPa, η^{ave}=0.50, $\Delta\beta$=0.34-0.36).

Figure

Click here to download Figure Figure 12.tif

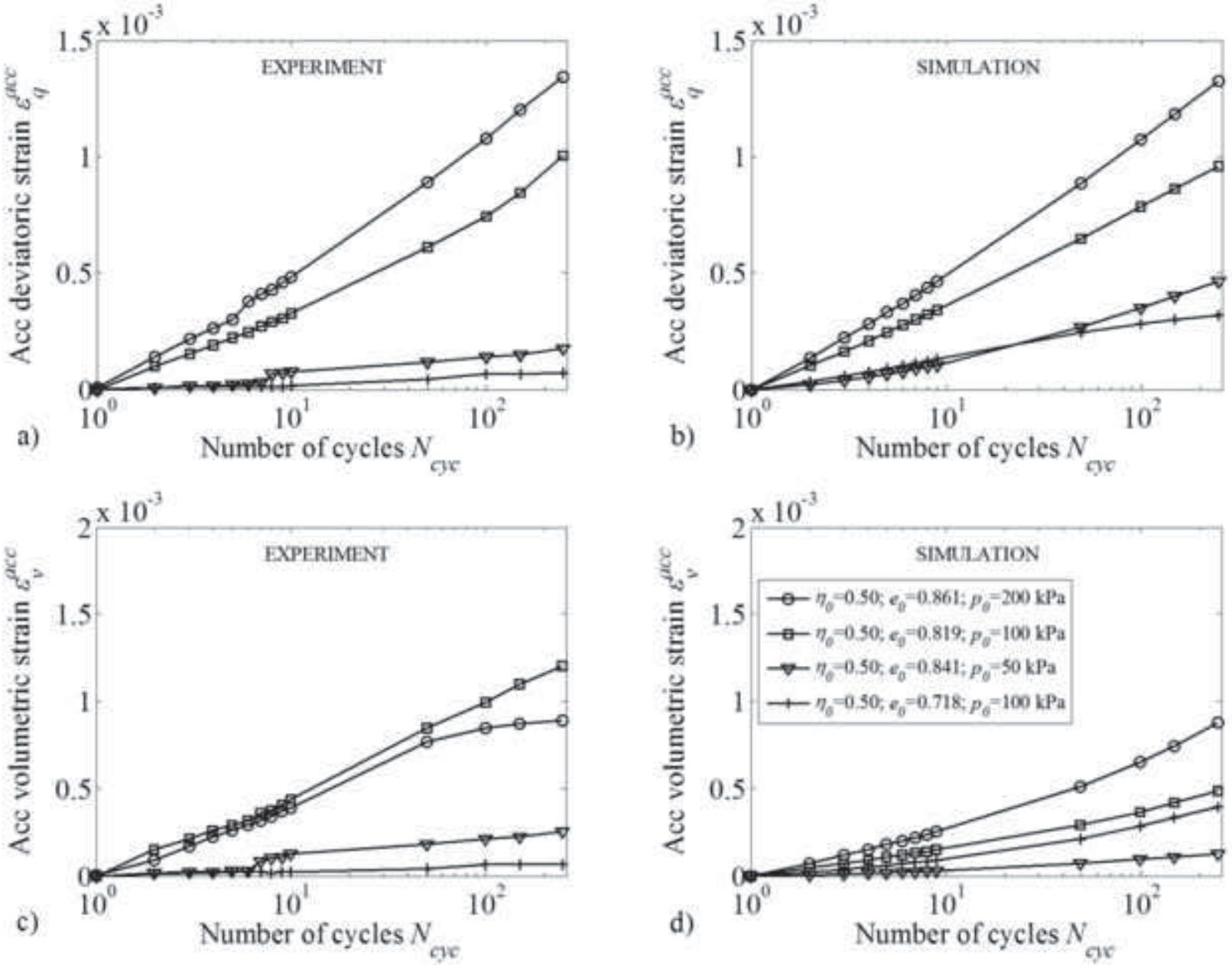

Fig. 12. Progressive strain accumulation with the number of cycles for dense samples a) experimental deviatoric strain accumulation b) simulation of deviatoric strain accumulations c) experimental volumetric strain accumulation d) simulation of volumetric strain accumulations ($\Delta\beta$=0.33-0.47).

Figure

Click here to download Figure Figure 13.tif

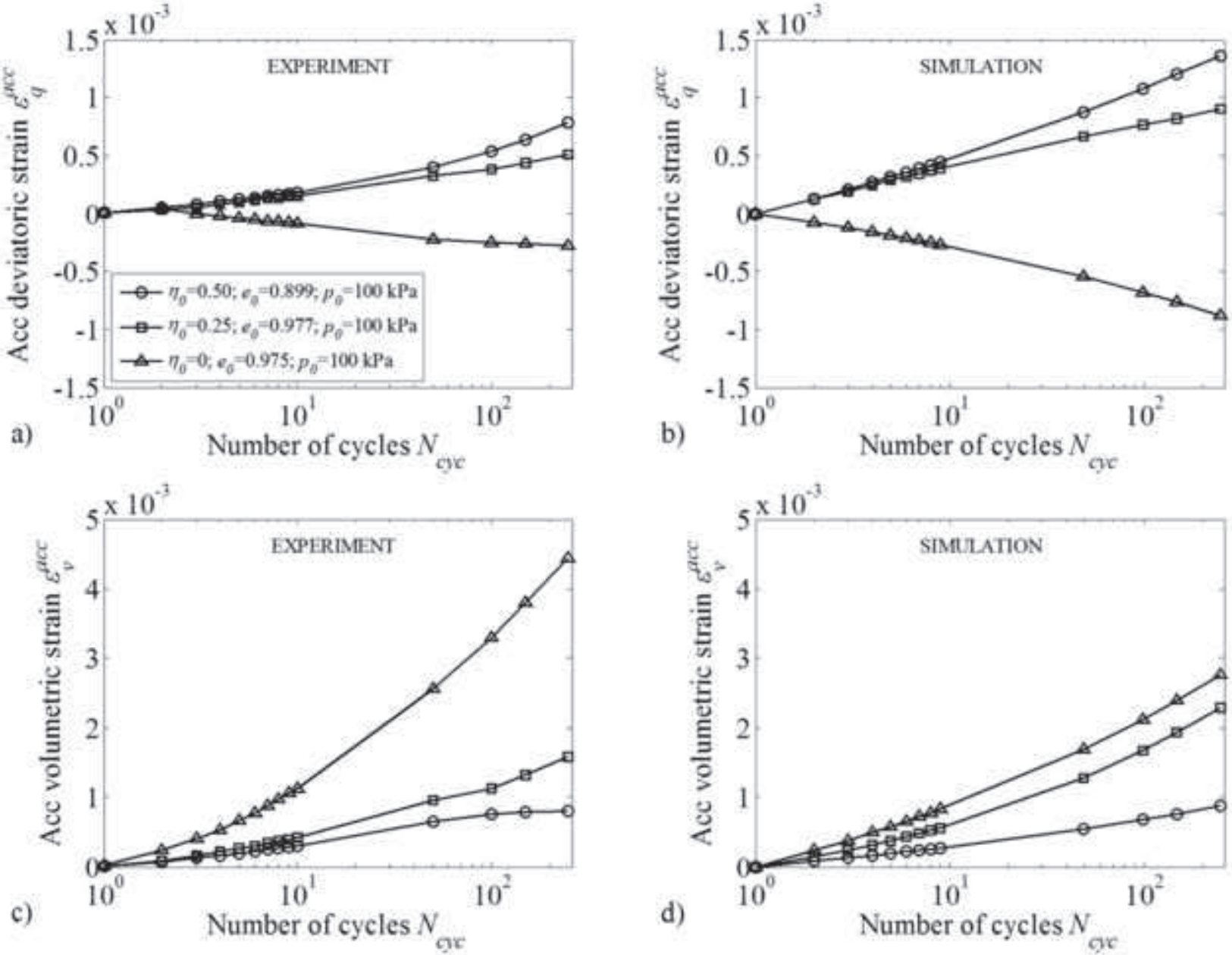

Fig. 13. Progressive strain accumulation with the number of cycles for loose samples a) experimental deviatoric strain accumulation b) simulation of deviatoric strain accumulations c) experimental volumetric strain accumulation d) simulation of volumetric strain accumulations ($\Delta\beta$=0.31-0.35).

Figure

Click here to download Figure Figure 14.tif

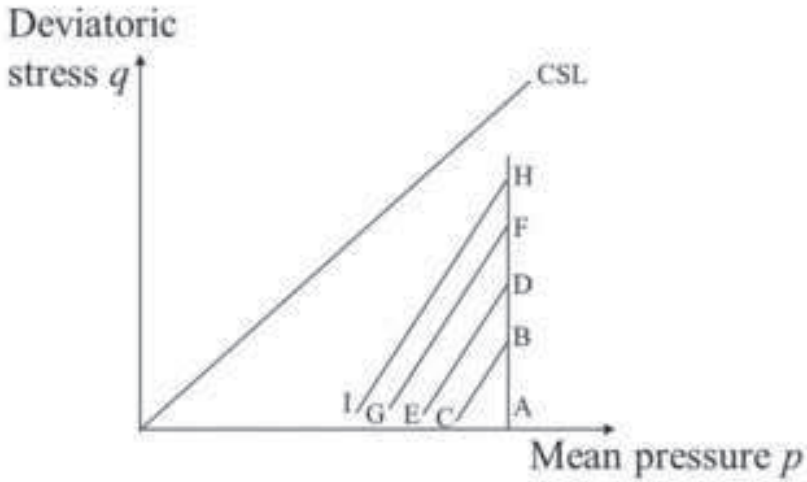

Fig. 14: Schematic representation of the stress path adopted in the test performed at different cyclic amplitudes. Testing conditions: e_0=0.824 and p_0=100 kPa with η^B=0.2, η^D=0.5, η^F=0.7 and η^H=0.9. Monotonic loading applied in the stages AB, BD, DF and FH and cyclic loading applied in the stages BC, DE, FG and FI imposing $\Delta\beta^{BC}$=0.18 for N_{cyc}=50, $\Delta\beta^{DE}$=0.48 for N_{cyc}=5, $\Delta\beta^{FG}$=0.62 for N_{cyc}=10 and $\Delta\beta^{HI}$=0.84 for N_{cyc}=10.

Figure

Click here to download Figure Figure 15.tif

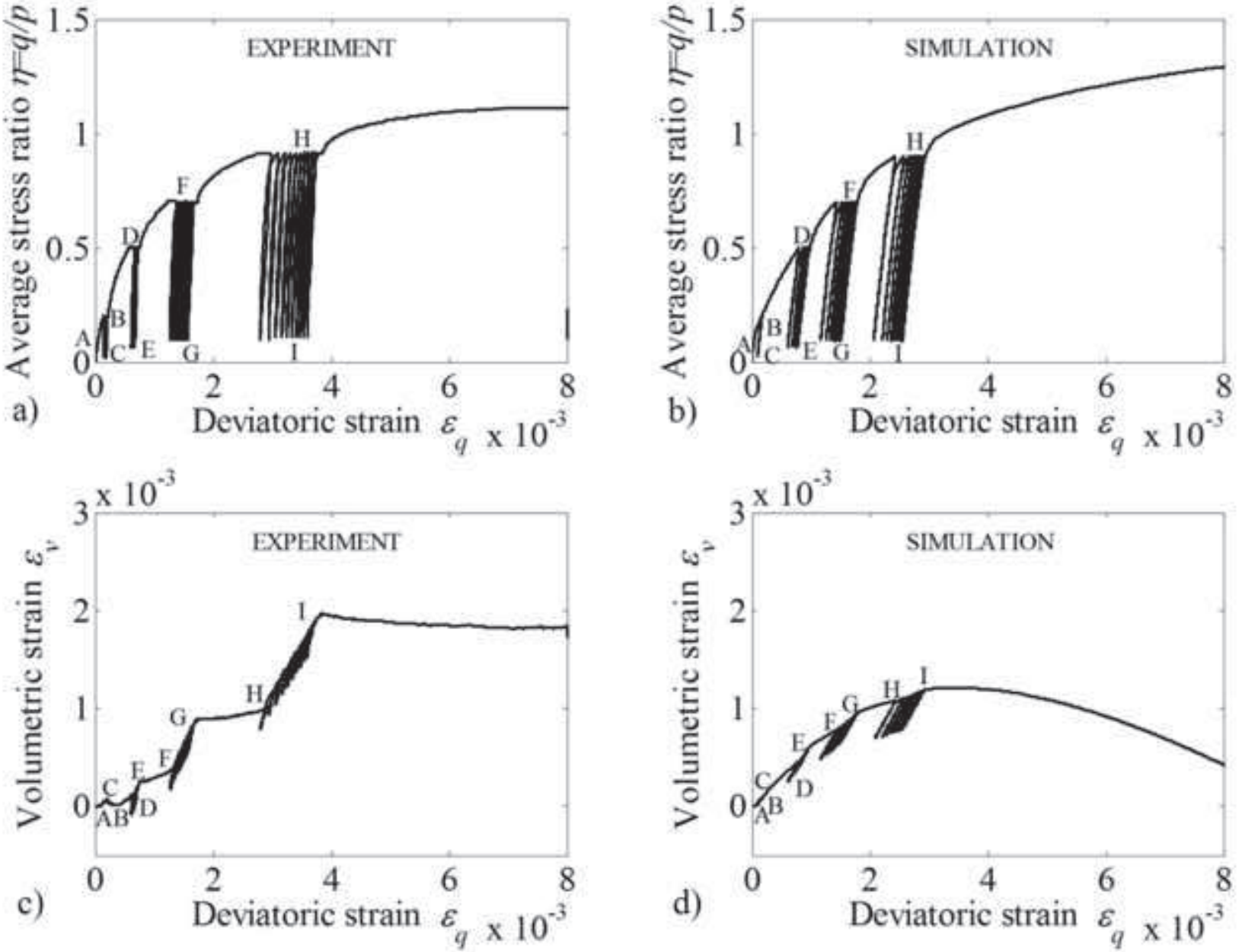

Fig. 15: Soil response while subjected to varying cyclic amplitude at different average stress ratios a) experimental stress strain response b) stress strain response from simulation c) experimental volumetric response and related d) simulation.